

Transverse-energy distributions at midrapidity in $p+p$, $d+Au$, and $Au+Au$ collisions at $\sqrt{s_{NN}} = 62.4\text{--}200$ GeV and implications for particle-production models.

S.S. Adler,⁷ S. Afanasiev,²⁴ C. Aidala,^{12,36} N.N. Ajitanand,⁵³ Y. Akiba,^{26,47,48} A. Al-Jamel,⁴¹ J. Alexander,⁵³ K. Aoki,^{29,47} L. Aphecetche,⁵⁵ R. Armendariz,⁴¹ S.H. Aronson,⁷ R. Averbeck,⁵⁴ T.C. Awes,⁴³ B. Azmoun,⁷ V. Babintsev,¹⁹ A. Baldisseri,¹³ K.N. Barish,⁸ P.D. Barnes,^{33,*} B. Bassalleck,⁴⁰ S. Bathe,^{6,8,37} S. Batsouli,¹² V. Baublis,⁴⁶ F. Bauer,⁸ A. Bazilevsky,^{7,48} S. Belikov,^{7,19,22,*} R. Bennett,⁵⁴ Y. Berdnikov,⁵⁰ M.T. Bjornedal,¹² J.G. Boissevain,³³ H. Borel,¹³ K. Boyle,⁵⁴ M.L. Brooks,³³ D.S. Brown,⁴¹ N. Bruner,⁴⁰ D. Bucher,³⁷ H. Buesching,^{7,37} V. Bumazhnov,¹⁹ G. Bunce,^{7,48} J.M. Burward-Hoy,^{32,33} S. Butsyk,⁵⁴ X. Camard,⁵⁵ S. Campbell,⁵⁴ J.-S. Chai,²⁵ P. Chand,⁵ W.C. Chang,² S. Chernichenko,¹⁹ C.Y. Chi,¹² J. Chiba,²⁶ M. Chiu,¹² I.J. Choi,⁶³ R.K. Choudhury,⁵ T. Chujo,^{7,59} V. Cianciolo,⁴³ C.R. Clevén,¹⁷ Y. Cobigo,¹³ B.A. Cole,¹² M.P. Comets,⁴⁴ P. Constantin,²² M. Csanád,¹⁵ T. Csörgő,⁶² J.P. Cussonneau,⁵⁵ T. Dahms,⁵⁴ K. Das,¹⁶ G. David,⁷ F. Deák,¹⁵ H. Delagrange,⁵⁵ A. Denisov,¹⁹ D. d'Enterria,¹² A. Deshpande,^{48,54} E.J. Desmond,⁷ A. Devismes,⁵⁴ O. Dietzsch,⁵¹ A. Dion,⁵⁴ J.L. Drachenberg,¹ O. Drapier,³⁰ A. Drees,⁵⁴ A.K. Dubey,⁶¹ A. Durum,¹⁹ D. Dutta,⁵ V. Dzhordzhadze,⁵⁶ Y.V. Efremenko,⁴³ J. Egdemir,⁵⁴ A. Enokizono,¹⁸ H. En'yo,^{47,48} B. Espagnon,⁴⁴ S. Esumi,⁵⁸ D.E. Fields,^{40,48} C. Finck,⁵⁵ F. Fleuret,³⁰ S.L. Fokin,²⁸ B. Forestier,³⁴ B.D. Fox,⁴⁸ Z. Fraenkel,^{61,*} J.E. Frantz,^{12,42} A. Franz,⁷ A.D. Frawley,¹⁶ Y. Fukao,^{29,47,48} S.-Y. Fung,⁸ S. Gadrat,³⁴ F. Gastineau,⁵⁵ M. Germain,⁵⁵ A. Glenn,⁵⁶ M. Gonin,³⁰ J. Gosset,¹³ Y. Goto,^{47,48} R. Granier de Cassagnac,³⁰ N. Grau,^{3,22} S.V. Greene,⁵⁹ M. Grosse Perdekamp,^{20,48} T. Gunji,¹⁰ H.-Å. Gustafsson,^{35,*} T. Hachiya,^{18,47} A. Hadj Henni,⁵⁵ J.S. Haggerty,⁷ M.N. Hagiwara,¹ H. Hamagaki,¹⁰ A.G. Hansen,³³ H. Harada,¹⁸ E.P. Hartouni,³² K. Haruna,¹⁸ M. Harvey,⁷ E. Haslum,³⁵ K. Hasuko,⁴⁷ R. Hayano,¹⁰ X. He,¹⁷ M. Heffner,³² T.K. Hemmick,⁵⁴ J.M. Heuser,⁴⁷ P. Hidas,⁶² H. Hiejima,²⁰ J.C. Hill,²² R. Hobbs,⁴⁰ M. Holmes,⁵⁹ W. Holzmann,⁵³ K. Homma,¹⁸ B. Hong,²⁷ A. Hoover,⁴¹ T. Horaguchi,^{47,48,57} M.G. Hur,²⁵ T. Ichihara,^{47,48} H. Inuma,^{29,47} V.V. Ikonnikov,²⁸ K. Imai,^{23,29,47} M. Inaba,⁵⁸ M. Inuzuka,¹⁰ D. Isenhower,¹ L. Isenhower,¹ M. Ishihara,⁴⁷ T. Isobe,¹⁰ M. Issah,⁵³ A. Isupov,²⁴ B.V. Jacak,⁵⁴ J. Jia,^{12,54} J. Jin,¹² O. Jinnouchi,^{47,48} B.M. Johnson,⁷ S.C. Johnson,³² K.S. Joo,³⁸ D. Jouan,⁴⁴ F. Kajihara,^{10,47} S. Kametani,^{10,60} N. Kamihara,^{47,57} M. Kaneta,⁴⁸ J.H. Kang,⁶³ K. Katou,⁶⁰ T. Kawabata,¹⁰ T. Kawagishi,⁵⁸ A.V. Kazantsev,²⁸ S. Kelly,^{11,12} B. Khachaturov,⁶¹ A. Khanzadeev,⁴⁶ J. Kikuchi,⁶⁰ D.J. Kim,⁶³ E. Kim,⁵² E.J. Kim,⁵² G.-B. Kim,³⁰ H.J. Kim,⁶³ Y.-S. Kim,²⁵ E. Kinney,¹¹ Á. Kiss,¹⁵ E. Kistenev,⁷ A. Kiyomichi,⁴⁷ C. Klein-Boesing,³⁷ H. Kobayashi,⁴⁸ L. Kochenda,⁴⁶ V. Kochetkov,¹⁹ R. Kohara,¹⁸ B. Komkov,⁴⁶ M. Konno,⁵⁸ D. Kotchetkov,⁸ A. Kozlov,⁶¹ P.J. Kroon,⁷ C.H. Kuberg,^{1,*} G.J. Kunde,³³ N. Kurihara,¹⁰ K. Kurita,^{47,49} M.J. Kweon,²⁷ Y. Kwon,⁶³ G.S. Kyle,⁴¹ R. Lacey,⁵³ J.G. Lajoie,²² A. Lebedev,^{22,28} Y. Le Bornec,⁴⁴ S. Leckey,⁵⁴ D.M. Lee,³³ M.K. Lee,⁶³ M.J. Leitch,³³ M.A.L. Leite,⁵¹ X.H. Li,⁸ H. Lim,⁵² A. Litvinenko,²⁴ M.X. Liu,³³ C.F. Maguire,⁵⁹ Y.I. Makdisi,⁷ A. Malakhov,²⁴ M.D. Malik,⁴⁰ V.I. Manko,²⁸ Y. Mao,^{45,47} G. Martinez,⁵⁵ H. Masui,⁵⁸ F. Matathias,⁵⁴ T. Matsumoto,^{10,60} M.C. McCain,^{1,20} P.L. McGaughey,³³ Y. Miake,⁵⁸ T.E. Miller,⁵⁹ A. Milov,⁵⁴ S. Mioduszewski,⁷ G.C. Mishra,¹⁷ J.T. Mitchell,⁷ A.K. Mohanty,⁵ D.P. Morrison,^{7,†} J.M. Moss,³³ T.V. Moukhanova,²⁸ D. Mukhopadhyay,^{59,61} M. Muniruzzaman,⁸ J. Murata,^{47,49} S. Nagamiya,²⁶ Y. Nagata,⁵⁸ J.L. Nagle,^{11,12,‡} M. Naglis,⁶¹ T. Nakamura,¹⁸ J. Newby,^{32,56} M. Nguyen,⁵⁴ B.E. Norman,³³ A.S. Nyanin,²⁸ J. Nystrand,³⁵ E. O'Brien,⁷ C.A. Ogilvie,²² H. Ohnishi,⁴⁷ I.D. Ojha,^{4,59} K. Okada,^{47,48} O.O. Omiwade,¹ A. Oskarsson,³⁵ I. Otterlund,³⁵ K. Oyama,¹⁰ K. Ozawa,¹⁰ D. Pal,^{59,61} A.P.T. Palounek,³³ V. Pantuev,^{21,54} V. Papavassiliou,⁴¹ J. Park,⁵² W.J. Park,²⁷ S.F. Pate,⁴¹ H. Pei,²² V. Penev,²⁴ J.-C. Peng,²⁰ H. Pereira,¹³ V. Peresedov,²⁴ D.Yu. Peressounko,²⁸ A. Pierson,⁴⁰ C. Pinkenburg,⁷ R.P. Pisani,⁷ M.L. Purschke,⁷ A.K. Purwar,⁵⁴ H. Qu,¹⁷ J.M. Qualls,¹ J. Rak,²² I. Ravinovich,⁶¹ K.F. Read,^{43,56} M. Reuter,⁵⁴ K. Reygers,³⁷ V. Riabov,⁴⁶ Y. Riabov,⁴⁶ G. Roche,³⁴ A. Romana,^{30,*} M. Rosati,²² S.S.E. Rosendahl,³⁵ P. Rosnet,³⁴ P. Rukoyatkin,²⁴ V.L. Rykov,⁴⁷ S.S. Ryu,⁶³ B. Sahlmueller,^{37,54} N. Saito,^{29,47,48} T. Sakaguchi,^{10,60} S. Sakai,⁵⁸ V. Samsonov,⁴⁶ L. Sanfratello,⁴⁰ R. Santo,³⁷ H.D. Sato,^{29,47} S. Sato,^{7,23,26,58} S. Sawada,²⁶ Y. Schutz,⁵⁵ V. Semenov,¹⁹ R. Seto,⁸ D. Sharma,⁶¹ T.K. Shea,⁷ I. Shein,¹⁹ T.-A. Shibata,^{47,57} K. Shigaki,¹⁸ M. Shimomura,⁵⁸ T. Shohjoh,⁵⁸ K. Shoji,^{29,47} A. Sickles,⁵⁴ C.L. Silva,⁵¹ D. Silvermyr,^{33,43} K.S. Sim,²⁷ C.P. Singh,⁴ V. Singh,⁴ S. Skutnik,²² W.C. Smith,¹ A. Soldatov,¹⁹ R.A. Soltz,³² W.E. Sondheim,³³ S.P. Sorensen,⁵⁶ I.V. Sourikova,⁷ F. Staley,¹³ P.W. Stankus,⁴³ E. Stenlund,³⁵ M. Stepanov,⁴¹ A. Ster,⁶² S.P. Stoll,⁷ T. Sugitate,¹⁸ C. Suire,⁴⁴ J.P. Sullivan,³³ J. Sziklai,⁶² T. Tabaru,⁴⁸ S. Takagi,⁵⁸ E.M. Takagui,⁵¹ A. Taketani,^{47,48} K.H. Tanaka,²⁶ Y. Tanaka,³⁹ K. Tanida,^{47,48,52} M.J. Tannenbaum,⁷ A. Taranenko,⁵³ P. Tarján,¹⁴ T.L. Thomas,⁴⁰ M. Togawa,^{29,47} J. Tojo,⁴⁷ H. Torii,^{29,47,48} R.S. Towell,¹ V.-N. Tram,³⁰ I. Tserruya,⁶¹ Y. Tsuchimoto,^{18,47} S.K. Tuli,^{4,*} H. Tydesjö,³⁵ N. Tyurin,¹⁹ T.J. Uam,³⁸ C. Vale,²² H. Valle,⁵⁹ H.W. van Hecke,³³ J. Velkovska,^{7,59} M. Velkovsky,⁵⁴ R. Vértesi,¹⁴ V. Veszprémi,¹⁴ A.A. Vinogradov,²⁸ M.A. Volkov,²⁸ E. Vznuzdaev,⁴⁶ M. Wagner,^{29,47}

X.R. Wang,^{17,41} Y. Watanabe,^{47,48} J. Wessels,³⁷ S.N. White,⁷ N. Willis,⁴⁴ D. Winter,¹² F.K. Wohn,²²
 C.L. Woody,⁷ M. Wysocki,¹¹ W. Xie,^{8,48} A. Yanovich,¹⁹ S. Yokkaichi,^{47,48} G.R. Young,⁴³ I. Younus,^{31,40}
 I.E. Yushmanov,²⁸ W.A. Zajc,¹² O. Zaudtke,³⁷ C. Zhang,¹² S. Zhou,⁹ J. Zimányi,^{62,*} L. Zolin,²⁴ and X. Zong²²

(PHENIX Collaboration)

- ¹Abilene Christian University, Abilene, Texas 79699, USA
²Institute of Physics, Academia Sinica, Taipei 11529, Taiwan
³Department of Physics, Augustana College, Sioux Falls, South Dakota 57197, USA
⁴Department of Physics, Banaras Hindu University, Varanasi 221005, India
⁵Bhabha Atomic Research Centre, Bombay 400 085, India
⁶Baruch College, City University of New York, New York, New York, 10010 USA
⁷Brookhaven National Laboratory, Upton, New York 11973-5000, USA
⁸University of California - Riverside, Riverside, California 92521, USA
⁹Science and Technology on Nuclear Data Laboratory, China Institute of Atomic Energy, Beijing 102413, P. R. China
¹⁰Center for Nuclear Study, Graduate School of Science, University of Tokyo, 7-3-1 Hongo, Bunkyo, Tokyo 113-0033, Japan
¹¹University of Colorado, Boulder, Colorado 80309, USA
¹²Columbia University, New York, New York 10027 and Nevis Laboratories, Irvington, New York 10533, USA
¹³Dapnia, CEA Saclay, F-91191, Gif-sur-Yvette, France
¹⁴Debrecen University, H-4010 Debrecen, Egyetem tér 1, Hungary
¹⁵ELTE, Eötvös Loránd University, H - 1117 Budapest, Pázmány P. s. 1/A, Hungary
¹⁶Florida State University, Tallahassee, Florida 32306, USA
¹⁷Georgia State University, Atlanta, Georgia 30303, USA
¹⁸Hiroshima University, Kagamiyama, Higashi-Hiroshima 739-8526, Japan
¹⁹IHEP Protvino, State Research Center of Russian Federation, Institute for High Energy Physics, Protvino, 142281, Russia
²⁰University of Illinois at Urbana-Champaign, Urbana, Illinois 61801, USA
²¹Institute for Nuclear Research of the Russian Academy of Sciences, prospect 60-letiya Oktyabrya 7a, Moscow 117312, Russia
²²Iowa State University, Ames, Iowa 50011, USA
²³Advanced Science Research Center, Japan Atomic Energy Agency, 2-4 Shirakata Shirane, Tokai-mura, Naka-gun, Ibaraki-ken 319-1195, Japan
²⁴Joint Institute for Nuclear Research, 141980 Dubna, Moscow Region, Russia
²⁵KAERI, Cyclotron Application Laboratory, Seoul, Korea
²⁶KEK, High Energy Accelerator Research Organization, Tsukuba, Ibaraki 305-0801, Japan
²⁷Korea University, Seoul, 136-701, Korea
²⁸Russian Research Center "Kurchatov Institute", Moscow, 123098 Russia
²⁹Kyoto University, Kyoto 606-8502, Japan
³⁰Laboratoire Leprince-Ringuet, Ecole Polytechnique, CNRS-IN2P3, Route de Saclay, F-91128, Palaiseau, France
³¹Physics Department, Lahore University of Management Sciences, Lahore, Pakistan
³²Lawrence Livermore National Laboratory, Livermore, California 94550, USA
³³Los Alamos National Laboratory, Los Alamos, New Mexico 87545, USA
³⁴LPC, Université Blaise Pascal, CNRS-IN2P3, Clermont-Fd, 63177 Aubiere Cedex, France
³⁵Department of Physics, Lund University, Box 118, SE-221 00 Lund, Sweden
³⁶Department of Physics, University of Michigan, Ann Arbor, Michigan 48109-1040, USA
³⁷Institut für Kernphysik, University of Muenster, D-48149 Muenster, Germany
³⁸Myongji University, Yongin, Kyonggido 449-728, Korea
³⁹Nagasaki Institute of Applied Science, Nagasaki-shi, Nagasaki 851-0193, Japan
⁴⁰University of New Mexico, Albuquerque, New Mexico 87131, USA
⁴¹New Mexico State University, Las Cruces, New Mexico 88003, USA
⁴²Department of Physics and Astronomy, Ohio University, Athens, Ohio 45701, USA
⁴³Oak Ridge National Laboratory, Oak Ridge, Tennessee 37831, USA
⁴⁴IPN-Orsay, Université Paris Sud, CNRS-IN2P3, BP1, F-91406, Orsay, France
⁴⁵Peking University, Beijing 100871, P. R. China
⁴⁶PNPI, Petersburg Nuclear Physics Institute, Gatchina, Leningrad region, 188300, Russia
⁴⁷RIKEN Nishina Center for Accelerator-Based Science, Wako, Saitama 351-0198, Japan
⁴⁸RIKEN BNL Research Center, Brookhaven National Laboratory, Upton, New York 11973-5000, USA
⁴⁹Physics Department, Rikkyo University, 3-34-1 Nishi-Ikebukuro, Toshima, Tokyo 171-8501, Japan
⁵⁰Saint Petersburg State Polytechnic University, St. Petersburg, 195251 Russia
⁵¹Universidade de São Paulo, Instituto de Física, Caixa Postal 66318, São Paulo CEP05315-970, Brazil
⁵²Seoul National University, Seoul, Korea
⁵³Chemistry Department, Stony Brook University, SUNY, Stony Brook, New York 11794-3400, USA
⁵⁴Department of Physics and Astronomy, Stony Brook University, SUNY, Stony Brook, New York 11794-3400, USA
⁵⁵SUBATECH (Ecole des Mines de Nantes, CNRS-IN2P3, Université de Nantes) BP 20722 - 44307, Nantes, France
⁵⁶University of Tennessee, Knoxville, Tennessee 37996, USA
⁵⁷Department of Physics, Tokyo Institute of Technology, Oh-okayama, Meguro, Tokyo 152-8551, Japan
⁵⁸Institute of Physics, University of Tsukuba, Tsukuba, Ibaraki 305, Japan

⁵⁹Vanderbilt University, Nashville, Tennessee 37235, USA

⁶⁰Waseda University, Advanced Research Institute for Science and Engineering, 17 Kikui-cho, Shinjuku-ku, Tokyo 162-0044, Japan

⁶¹Weizmann Institute, Rehovot 76100, Israel

⁶²Institute for Particle and Nuclear Physics, Wigner Research Centre for Physics, Hungarian Academy of Sciences (Wigner RCP, RMKI) H-1525 Budapest 114, POBox 49, Budapest, Hungary

⁶³Yonsei University, IPAP, Seoul 120-749, Korea

(Dated: November 6, 2018)

Measurements of the midrapidity transverse energy distribution, $dE_T/d\eta$, are presented for $p+p$, $d+Au$, and $Au+Au$ collisions at $\sqrt{s_{NN}} = 200$ GeV and additionally for $Au+Au$ collisions at $\sqrt{s_{NN}} = 62.4$ and 130 GeV. The $dE_T/d\eta$ distributions are first compared with the number of nucleon participants N_{part} , number of binary collisions N_{coll} , and number of constituent-quark participants N_{qp} calculated from a Glauber model based on the nuclear geometry. For $Au+Au$, $\langle dE_T/d\eta \rangle / N_{\text{part}}$ increases with N_{part} , while $\langle dE_T/d\eta \rangle / N_{qp}$ is approximately constant for all three energies. This indicates that the two component ansatz, $dE_T/d\eta \propto (1-x)N_{\text{part}}/2 + xN_{\text{coll}}$, which has been used to represent E_T distributions, is simply a proxy for N_{qp} , and that the N_{coll} term does not represent a hard-scattering component in E_T distributions. The $dE_T/d\eta$ distributions of $Au+Au$ and $d+Au$ are then calculated from the measured $p+p$ E_T distribution using two models that both reproduce the $Au+Au$ data. However, while the number-of-constituent-quark-participant model agrees well with the $d+Au$ data, the additive-quark model does not.

PACS numbers: 25.75.Dw

I. INTRODUCTION

Measurements of midrapidity transverse energy distributions $dE_T/d\eta$ in $p+p$, $d+Au$ and $Au+Au$ collisions at $\sqrt{s_{NN}} = 200$ GeV and $Au+Au$ collisions at $\sqrt{s_{NN}} = 62.4$ and 130 GeV are presented. The transverse energy E_T is a multiparticle variable defined as the sum

$$E_T = \sum_i E_i \sin \theta_i \quad (1)$$

$$dE_T(\eta)/d\eta = \sin \theta(\eta) dE(\eta)/d\eta, \quad (2)$$

where θ is the polar angle, $\eta = -\ln \tan \theta/2$ is the pseudorapidity, E_i is by convention taken as the kinetic energy for baryons, the kinetic energy + $2 m_N$ for antibaryons, and the total energy for all other particles, and the sum is taken over all particles emitted into a fixed solid angle for each event. In the present measurement as in previous measurements [1, 2] the raw E_T , denoted $E_{T\text{EMC}}$, is measured in five sectors of the PHENIX lead-scintillator (PbSc) electromagnetic calorimeter (EMCal) [1] which cover the solid angle $|\eta| \leq 0.38$, $\Delta\phi = 90^\circ + 22.5^\circ$, and is corrected to total hadronic E_T , more properly $dE_T/d\eta|_{\eta=0}$, within a reference acceptance of $\Delta\eta = 1.0$, $\Delta\phi = 2\pi$ (details are given in section IV).

The significance of systematic measurements of midrapidity $dE_T/d\eta$ and the closely related charged particle multiplicity distributions, $dN_{\text{ch}}/d\eta$, as a function of A

and B in $A+B$ collisions is that they provide excellent characterization of the nuclear geometry of the reaction on an event-by-event basis, and are sensitive to the underlying reaction dynamics, which is the fundamental element of particle emission in $p+p$ and $A+B$ collisions at a given $\sqrt{s_{NN}}$. For instance, measurements of $dN_{\text{ch}}/d\eta$ in $Au+Au$ collisions at the Relativistic Heavy Ion Collider (RHIC), as a function of centrality expressed as the number of participating nucleons, N_{part} , do not depend linearly on N_{part} but have a nonlinear increase of $\langle dN_{\text{ch}}/d\eta \rangle$ with increasing N_{part} . The nonlinearity has been explained by a two component model [3, 4] proportional to a linear combination of N_{coll} and N_{part} , with the implication that the N_{coll} term represents a contribution from hard scattering. Alternatively, it has been proposed that $dN_{\text{ch}}/d\eta$ is linearly proportional to the number of constituent-quark participants (NQP) model [5], without need to introduce a hard-scattering component. For symmetric systems, the NQP model is identical to the Additive Quark Model (AQM) [6] used in the 1980's, to explain the similar nonproportionality of $dE_T/d\eta$ with N_{part} in $\alpha - \alpha$ compared to $p+p$ collisions at $\sqrt{s_{NN}} = 31$ GeV [7]. In the AQM, constituent-quark participants in the two colliding nuclei are connected by color-strings; but with the restriction that only one color-string can be attached to a quark-participant. At midrapidity, the transverse energy production is proportional to the number of color-strings spanning between the projectile and the target nuclei. For asymmetric systems, such as $d+Au$, the models differ because the number of color-strings is proportional only to the number of quark-participants in the projectile (the lighter nucleus). For symmetric $A+A$ collisions, the number of quark-participants in the target is the same as number of quark-participants in the projectile, so the AQM is equivalent to the NQP model. These models will be described in

*Deceased

†PHENIX Co-Spokesperson: morrison@bnl.gov

‡PHENIX Co-Spokesperson: jamie.nagle@colorado.edu

detail and tested with the present data.

II. PREVIOUS MEASUREMENTS—A HISTORICAL PERSPECTIVE

A. Charged Multiplicity Distributions

The charged particle multiplicity or multiplicity density in rapidity, dN_{ch}/dy , is one of the earliest descriptive variables in high energy particle and nuclear physics dating from cosmic-ray studies [8]. An important regularity first observed in cosmic rays was that the produced pions have limited transverse momentum with respect to the collision axis, exponentially decreasing as e^{-6p_T} , commonly known as the ‘‘Cocconi Formula’’ [9, 10].

By the early 1970’s the framework for the study of this ‘‘soft’’ multi-particle physics was well in place. One of the important conceptual breakthroughs was the realization that the distribution of multiplicity for multiple particle production would not be Poisson unless the particles were emitted independently, without any correlation, but that short-range rapidity correlations were expected as a consequence of ‘‘Regge-Pole-dominated’’ reactions [11]. In fact, in marked deviation from Poisson behavior, the total charged particle multiplicity distributions appeared to exhibit a universal form, ‘‘KNO scaling’’ [12] (or ‘‘scaling in the mean’’), when ‘‘scaled’’ at each \sqrt{s} by the average multiplicity—i.e. dN_{ch}/dz was a universal function of the scaled multiplicity, $z \equiv N_{\text{ch}}/\langle N_{\text{ch}} \rangle$, where $\langle N_{\text{ch}} \rangle$ is the mean multiplicity at a given \sqrt{s} [13]. In the mid 1980’s, the UA5 group at the CERN Super Proton Synchrotron collider discovered that KNO scaling did not hold in general [14], and found that their measured multiplicity distributions, both in limited rapidity intervals and over all phase space were described by negative binomial distributions (NBD), which since then have been shown to provide accurate descriptions for N_{ch} distributions from high energy collisions of both particles and nuclei.

Also in this period, the central plateau of the rapidity distribution of identified charged particles, $dN_{\text{ch}}(y)/dy$, was discovered at the CERN-ISR [15]. Along with this discovery came the first interest to measure the multiplicity distribution in a restricted pseudorapidity range, $|\eta| \leq 1.5$, ‘‘wide enough to allow for good statistics, yet sufficiently remote from the edge of the rapidity plateau to permit specific analysis of the central region’’ [16]. The first suggestion to use multiplicity distributions in restricted regions of rapidity for the study of reaction dynamics, specifically quantum optical coherence effects in $p+p$ collisions, was made by Fowler and Weiner [17], who emphasized the importance of using small-regions, where energy-momentum-conservation constraints would not be significant.

B. E_T Distributions

The phenomenology of E_T measurements, which evolved over a similar time period as that of multiplicity distributions, was based initially on the search for the jets of hard-scattering in $p+p$ collisions in ‘‘ 4π -hadron calorimeters’’ as first proposed by Willis [18] and then by Bjorken [19], who specifically emphasized the need for the capability of measuring the total amount of energy emerging into small elements of solid angle to observe the event structure of what he called local cores (now jets) predicted for hard-scattering. Ochs and Stodolsky [20] later proposed the veto of energy by a calorimeter in the forward direction, which was elaborated by Landshoff and Polkinghorne [21] who coined the name ‘‘transverse energy’’: ‘‘The energy not observed in the forward direction due to hard-scattering processes would be emitted as ‘transverse energy’ ’’. The first experiment to measure an ‘‘ E_T distribution’’ corresponding to the terminology used at present was the NA5 experiment at CERN [22], which utilized a full azimuth hadronic calorimeter covering the region $-0.88 < \eta < 0.67$. They demonstrated that instead of finding jets [22], ‘‘The large E_T observed is the result of a large number of particles with a rather small transverse momentum.’’ The close relationship between E_T and multiplicity distributions was shown in a measurement by UA1 in $\bar{p}+p$ collisions at $\sqrt{s} = 540$ GeV at the CERN Super Proton Synchrotron collider [23], with a full azimuth ‘‘hermetic calorimeter’’ covering $|\Delta\eta| \leq 3$, which demonstrated that the ‘‘ E_T measured in the calorimeter was strongly correlated to the measured multiplicity’’ and that the KNO scaled E_T and N_{ch} distributions were ‘‘strikingly similar’’. Ironically, this was to be presented at the same meeting (ICHEP82) at which UA2 presented the discovery of dijets [24] in the region of a break in the steep exponential slope of an E_T distribution, to a flatter slope, 5–6 orders of magnitude down in cross section. Since then, it has been established that E_T and N_{ch} distributions are much less sensitive to hard-scattering than single inclusive measurements; and these distributions have been used to study the ‘‘soft’’ physics that dominates the $p+p$ inelastic cross section [25]. In fact, just a year after ICHEP82, Bjorken [26] stressed the importance of the region of the ‘‘central plateau’’ of rapidity for the study of the evolution of the Quark Gluon Plasma and proposed $dE_T/dy|_{y=0}$ as an estimate of the co-moving energy density in a longitudinal expansion, proportional to the energy density in space, called the Bjorken Energy Density:

$$\epsilon_{Bj} = \frac{dE_T}{dy} \frac{1}{\tau_0 \pi R^2} \quad (3)$$

where τ_0 , the formation time, is usually taken as 1 fm/c and πR^2 is the effective area of the collision. This formula is derived under the assumption that $\langle E_T \rangle$ per particle $\propto T$ for a thermal medium, which has nothing to do with hard scattering.

C. Collisions of Relativistic Nuclei-Extreme Independent Models

The first experiments specifically designed to measure the dependence of the charged particle multiplicity in high energy $p + A$ collisions as a function of the nuclear size were performed by Busza and collaborators [27] at Fermilab using beams of $\sim 50\text{--}200$ GeV/ c hadrons colliding with various fixed nuclear targets. They found the extraordinary result [27] that the charged particle multiplicity density, $dN_{\text{ch}}/d\eta$, observed in proton+nucleus ($p+A$) interactions was not simply proportional to the number of collisions, but increased much more slowly. The other striking observation [28] was that a relativistic incident proton could pass through e.g. $\nu = 4$ absorption-mean-free-paths of a target nucleus and emerge from the other side, and furthermore there was no intranuclear cascade of produced particles (a stark difference from what would happen to the same proton in a macroscopic 4 mean-free-path hadron calorimeter). In the forward fragmentation region of 200 GeV/ c $p+A$ collisions, within one unit of rapidity from the beam $y^{\text{beam}} = 6.0$, there was essentially no change in $dN_{\text{ch}}/d\eta$ as a function of A , while the peak of the distribution moved backwards from midrapidity ($y_{NN}^{\text{cm}} \sim 3.0$) with increasing A and the total multiplicity increased, resulting in a huge relative increase of multiplicity in the target fragmentation region, $\eta < 1$ in the laboratory system.

These striking features of the ~ 200 GeV/ c fixed target hadron-nucleus data ($\sqrt{s_{NN}} \sim 19.4$ GeV) showed the importance of taking into account the time and distance scales of the soft multi-particle production process including quantum mechanical effects [29–34]. The observations had clearly shown that the target nucleus was rather transparent, so that a relativistic incident nucleon could make many successive collisions while passing through the nucleus and emerge intact. Immediately after a relativistic nucleon interacts inside a nucleus, the only thing that can happen consistent with relativity and quantum mechanics is for it to become an excited nucleon with roughly the same energy and reduced longitudinal momentum and rapidity. The relativistic nucleon remains in that state inside the nucleus, because the uncertainty principle and time dilation prevent it from fragmenting into particles until it is well outside the nucleus. This feature immediately eliminates the possibility of a cascade in the nucleus from the rescattering of the secondary products. Making the further assumptions (1) that an excited nucleon interacts with the same cross section as an unexcited nucleon and (2) that the successive collisions of the excited nucleon do not affect the excited state or its eventual fragmentation products [35], leads to the conclusion that the elementary process for particle production in nuclear collisions is the excited nucleon. This also leads to the prediction that the multiplicity in nuclear interactions should be proportional to the total number of projectile and target participants, rather than to the total number of collisions, which is called the

wounded-nucleon model (WNM) [36]. Common usage is to refer to the wounded nucleons (WN) as participants.

Interestingly, at midrapidity, the WNM works well only at roughly $\sqrt{s_{NN}} \sim 20$ GeV where it was discovered. For $\sqrt{s_{NN}} \lesssim 5.4$ GeV, particle production is smaller than the WNM due to the large stopping [37] with reduced transparency; and the E_T distributions in $A+B$ collisions can be represented by sums of convolutions of the $p+A$ distribution according to the relative probability of the number of projectile participants, the wounded-projectile-nucleon model (WPNM) [38–40]. For $\sqrt{s_{NN}} \geq 31$ GeV, particle production is larger than the WNM [41, 42] and the AQM [6, 7], which is equivalent to a wounded-projectile-quark (color-string) model, has been used successfully. All three of the above models, as well as the models to be described below, are of the type referred to as extreme independent models (EIM). The effect of the nuclear geometry of the interaction can be calculated in EIMs, independently of the dynamics of particle production, which can be derived from experimental measurements, usually the $p+p$ (or $p+A$) measurement in the same detector. In fact, the first published measurements at the CERN [43] and BNL [44] fixed target heavy ion programs in 1986–87 were E_T distributions in which EIM, rather than cuts on centrality, were used to understand the data.

At RHIC ($\sqrt{s_{NN}} = 19.6\text{--}200$ GeV), PHOBOS [45] has shown that the WNM works in Au+Au collisions for the total multiplicity, N_{ch} , over the range $|\eta| < 5.4$, while at midrapidity, the WNM fails—the multiplicity density per participant pair, $\langle dN_{\text{ch}}/d\eta \rangle / (N_{\text{part}}/2)$, increases with increasing number of participants, in agreement with previous PHENIX results [1, 2, 46]. Additionally, it has been shown using PHOBOS Au+Au data [5, 47] and discussed for other data [48] that the midrapidity $\langle dN_{\text{ch}}/d\eta \rangle$ as a function of centrality in Au+Au collisions is linearly proportional to the NQP model; however for symmetric systems this cannot be distinguished from the number of color-strings, the AQM [49]. The present work completes the cycle and demonstrates, using midrapidity E_T distributions at $\sqrt{s_{NN}} = 200$ GeV in the asymmetric $d+Au$ system, as well as $p+p$ and Au+Au collisions, that the asymmetric $d+Au$ measurement, which is crucial in distinguishing the color-string AQM from NQP models, clearly rejects the AQM and agrees very well with the NQP model.

While the concept of nucleon participants in collisions of nuclei is straightforward to understand, the concept of constituent-quark participants needs some elaboration. The nonrelativistic constituent-quark model [50, 51] is the basis of understanding the observed spectrum of the meson and baryon elementary particles as bound states, i.e. $(q\bar{q})$ for mesons and (qqq) for baryons. In addition to the masses and quantum numbers, other static properties such as the magnetic moments of baryons are also predicted in this model (see Refs. [52, 53], and references therein). However, these constituent-quarks are not the nearly massless u and d quarks (partons),

called “current quarks” from their role in the currents of electroweak and QCD quantum field theories. The constituent-quarks are assumed to be complex objects or quasi-particles [54] made out of the point-like partons of QCD hard-scattering, the (current) quarks, anti-quarks and gluons. The constituent or valence quarks (valons) thus acquire masses on the order of $1/3$ the nucleon mass (or $1/2$ the ρ -meson mass), called “chiral symmetry breaking” [55, 56], when bound in the nucleon (or meson). According to Shuryak [54] (see also Ref. [57]), there are two scales for hadrons predicted in QCD, the confinement length given by the radii of hadrons, $R_{\text{conf}} \approx 1 \text{ fm} \approx R_{\text{hadron}}$, as well as objects at the scale $1/3$ smaller, the constituent-quarks (valons [58]). For instance, the consideration of constituent-quarks as ‘little bags’ with application to the σ_L/σ_T puzzle in deep inelastic lepton-hadron scattering and other hard processes was made by T. Akiba [59].

One other key feature of the constituent-quark model is additivity: the properties of a hadron are described as the independent sum of contributions of the individual quarks. In other words the three constituent-quarks in each nucleon in a nucleon-nucleon collision act like the three nucleons in each triton in a ${}^3\text{H}+{}^3\text{H}$ collision: i.e. apart from their spatial correlation, the three nucleons in each triton act independently in the collision. This additive quark assumption [57, 60, 61] gives the relation that the pion-nucleon total cross section is $2/3$ the nucleon-nucleon total cross section, i.e. $\sigma(\pi p)/\sigma(pp) = 2/3$. The constituent-quark participant (NQP) model is simply an extension of this idea to multiplicity and E_T distributions (“soft” multi-particle physics) in $p+p$, $p+A$ and $A+A$ collisions. Although proposed first [6], the AQM is a special case of the NQP model in which a color string connects two constituent-quarks which have scattered, and breaking of the color-string produces particles at midrapidity. However, in the AQM [6, 7], it is further assumed that multiple strings attached to the same projectile quark in a $p+A$ collision coalesce and collapse into one color string, so that the AQM is effectively a wounded projectile quark model.

In this paper, we compare extreme-independent models of soft multi-particle production based on the number of fundamental elements taken as nucleon participants, nuclear collisions, constituent quarks and color-strings (AQM) with our measurement of transverse energy production. It will be shown that the ansatz, $dE_T/d\eta \propto (1-x)N_{\text{part}}/2 + xN_{\text{coll}}$, does not imply that there is a hard scattering component in multi-particle production, consistent with the direct observations noted above. Thus, possible models motivated by the fact that half of the momentum of a nucleon is carried by gluons when probed at high Q^2 in hard-scattering are not considered and we limit our comparison to the nucleon and constituent-quark participant models of soft-multiparticle production widely used since the 1970’s as discussed in the introduction.

III. THE PHENIX DETECTOR

The PHENIX detector at Brookhaven National Laboratory’s RHIC comprises two central spectrometer arms and two muon spectrometer arms. A comprehensive description of the detector components and performance can be found elsewhere [62]. The analysis described here utilizes five of the PbSc EMCAL sectors [62] in the central arm spectrometers, as illustrated schematically in Figure 1. Each calorimeter sector covers a rapidity range of $|\eta| < 0.38$ and subtends 22.5° in azimuth for a total azimuthal coverage of 112.5° . Each sector, whose front face is 5.1 m from the beam axis, is comprised of 2,592 PbSc towers assembled in a 36×72 array. Each tower has a $5.535 \text{ cm} \times 5.535 \text{ cm}$ surface area and an active depth of 37.5 cm corresponding to 0.85 nuclear interaction lengths or 18 radiation lengths. The PbSc EMCAL energy resolution for test beam electrons is $\frac{\Delta E}{E} = \frac{8.1\%}{\sqrt{E(\text{GeV})}} \oplus 2.1\%$, with a measured response proportional to the incident electron energy to within $\pm 2\%$ over the range $0.3 \leq E_e \leq 40 \text{ GeV}$.

A minimum-bias (MB) trigger for Au+Au, d +Au, and p + p collisions is provided by two identical beam-beam counters (BBC), labeled North and South, each consisting of 64 individual Čerenkov counters. The BBCs cover the full azimuthal angle in the pseudorapidity range $3.0 < |\eta| < 3.9$ [63]. For $p+p$ and d +Au collisions, events are required to have at least one counter fire in both the North and South BBCs. For Au+Au collisions, at least two counters must fire in both BBCs. Timing information from the BBCs are used to reconstruct the event vertex with a resolution of 6 mm for central Au+Au collisions. All events are required to have an event vertex within 20 cm of the origin. Centrality determination in 200 GeV and 130 GeV Au+Au collisions [62] is based upon the total charge deposited in the BBCs and the total energy deposited in the Zero Degree Calorimeters (ZDC) [63], which are hadronic calorimeters covering the pseudorapidity range $|\eta| > 6$. For 62.4 GeV Au+Au collisions, only the BBCs are used to determine centrality due to the reduced acceptance of the ZDCs at lower energies [64].

Table I gives a summary of the 2003 and 2004 data sets used in this analysis. Previously, PHENIX has studied transverse energy production in Au+Au collisions at $\sqrt{s_{NN}} = 200 \text{ GeV}$, 130 GeV , and 19.6 GeV [1, 2] and shown that for E_T measurements at midrapidity at a collider the EMCAL acts as a thin but effective hadron calorimeter. Presented here is an extended analysis of 200 GeV Au+Au collision data taken during 2004 with the magnetic field turned on that increases the statistics of the previous analysis by a factor of 494 with 132.9 million MB events. These new results are consistent with the previously published results [1, 2].

The average luminosity delivered by RHIC has improved dramatically each year, by a factor of 5.75 for $p+p$ collisions and 4.5 for d +Au collisions from the 2003 to 2008 running periods. Due to the readout electronics

implemented for the EMCal, with a pile-up window of 428 nsec, the increased luminosity results in an increasing rate-dependent background in the minimum-bias event sample due to multiple collisions, or pile-up, that artificially raises the transverse energy recorded in an event. To minimize this background, the 200 GeV $p+p$ and 200 GeV $d+Au$ data samples presented here are from the earlier 2003 running period.

TABLE I: Summary of the data sets used in this analysis. N_{events} represents the number of MB events analyzed and \mathcal{L}_{ave} represents the average RHIC luminosity for the dataset.

$\sqrt{s_{NN}}$ (GeV)	System	Year	N_{events}	$\mathcal{L}_{\text{ave}} (cm^{-2} s^{-1})$
200	Au+Au	2004	132.9 M	5×10^{26}
62.4	Au+Au	2004	20.0 M	0.6×10^{26}
200	$d+Au$	2003	50.1 M	3×10^{28}
200	$p+p$	2003	14.6 M	4×10^{30}

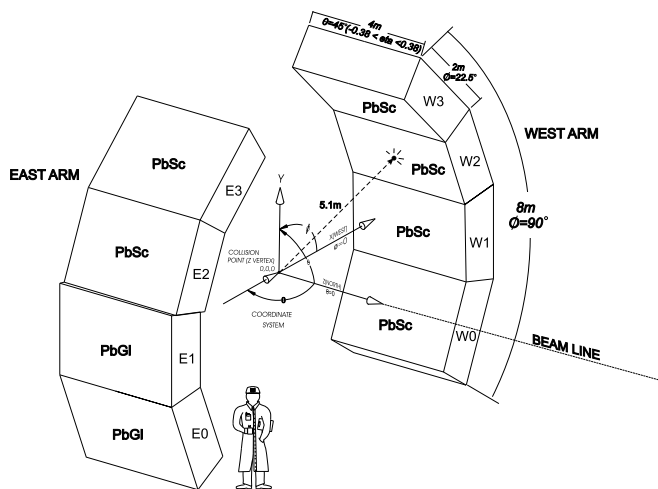


FIG. 1: Schematic diagram showing the locations of the PHENIX electromagnetic calorimeter sectors in the central arm spectrometer. The sectors labeled W1,W2,W3,E2 and E3 were used in this analysis

IV. DATA ANALYSIS

The analysis procedure for $dE_T/d\eta$ is described in detail in [2] and summarized here. The absolute energy scale for the PbSc EMCal was calibrated using the π^0 mass peak from pairs of reconstructed EMCal clusters. The uncertainty in the absolute energy scale is 2% in the 62.4 GeV Au+Au dataset and 1.5% in the 200 GeV Au+Au, $p+p$, and $d+Au$ datasets. The transverse energy for each event was computed using clusters with an energy greater than 30 MeV composed of adjacent towers each with a deposited energy of more than 10 MeV. Faulty towers and all towers in a 3×3 tower area around any faulty tower are excluded from the analysis.

The raw spectra of the measured transverse energy $E_{T\text{EMC}}$ in the fiducial aperture are given as histograms of the number of entries in a given raw $E_{T\text{EMC}}$ bin such that the total number of entries sums up to the number of BBC counts. The distributions are then normalized to integrate to unity. As an example, the $E_{T\text{EMC}}$ distributions as a function of centrality in 5% wide centrality bins are shown in Fig. 2 for 62.4 GeV Au+Au collisions.

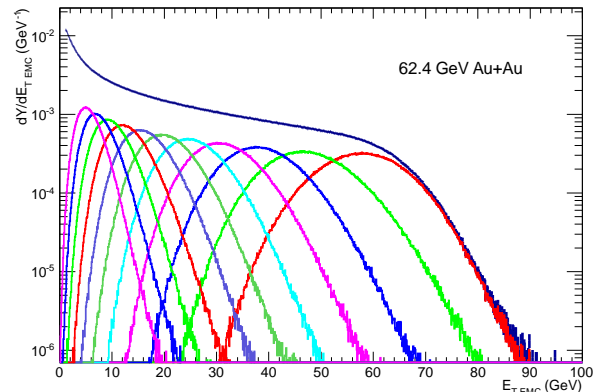


FIG. 2: (Color online) $E_{T\text{EMC}}$ distributions for $\sqrt{s_{NN}} = 62.4$ GeV Au+Au collisions. Shown are the MB distribution along with the distributions in 5% wide centrality bins selected using the BBCs. All the plots are normalized so that the integral of the MB distribution is unity.

To obtain the total hadronic E_T within a reference acceptance of $\Delta\eta = 1.0, \Delta\phi = 2\pi$, more properly $dE_T/d\eta|_{\eta=0}$, from the measured raw transverse energy, $E_{T\text{EMC}}$, several corrections are applied. The total correction can be decomposed into three main components. First is a correction by a factor of 4.188 to account for the fiducial acceptance. Second is a correction by a factor of 1.262 for 200 GeV Au+Au, 1.236 for 62.4 GeV Au+Au, 1.196 for 200 GeV $d+Au$, and 1.227 for 200 GeV $p+p$ to account for disabled calorimeter towers not used in the analysis. Third is a factor, k , which is the ratio of the total hadronic E_T in the fiducial aperture to the measured $E_{T\text{EMC}}$. Details on the estimate of the values of the k factor are given below. The total correction scale factors are obtained by multiplying these three components and are listed in Table II. The corrected MB distributions for 200 GeV Au+Au, $d+Au$, and $p+p$ are shown in Fig 3.

The k factor comprises three components. The first component, denoted k_{response} , is due to the fact that the EMCal was designed for the detection of electromagnetic particles [1]. Hadronic particles passing through the EMCal only deposit a fraction of their total energy. The average EMCal response is estimated for the various particle species using the HIJING event generator [65] processed through a GEANT-based Monte Carlo simulation of the PHENIX detector. The HIJING particle composition and p_T spectra are adjusted to reproduce the identified charged particle spectra and yields mea-

TABLE II: Summary of the total correction scale factors applied to the measured raw transverse energy, $E_{T\text{EMC}}$, to obtain $dE_T/d\eta|_{\eta=0}$ for each dataset.

$\sqrt{s_{NN}}$ (GeV)	System	Correction Factor
200	Au+Au	6.87 ± 0.40
62.4	Au+Au	6.73 ± 0.39
200	d +Au	6.51 ± 0.54
200	p + p	6.68 ± 0.56

sured by PHENIX. For all of the data sets, 75% of the total energy incident on the EMCAL is measured, thus $k_{\text{response}} = 1/0.75 = 1.33$. The second component of the k factor, denoted k_{inflow} , is a correction for energy inflow from outside the fiducial aperture of the EMCAL. This energy inflow arises from two sources: from parent particles with an original trajectory outside of the fiducial aperture whose decay products are incident within the fiducial aperture, and from particles that reflect off of the PHENIX magnet poles into the EMCAL fiducial aperture. The energy inflow contribution is 24% of the measured energy, thus $k_{\text{inflow}} = 1-0.24 = 0.76$. The third component of the k factor, denoted k_{losses} , is due to energy losses. There are three components to the energy loss: from particles with an original trajectory inside the fiducial aperture of the EMCAL whose decay products are outside of the fiducial aperture (10%), from energy losses at the edges of the EMCAL (6%), and from energy losses due to the energy thresholds (6%). The total contribution from energy losses is 22%, thus $k_{\text{losses}} = 1/(1-0.22) = 1.282$. The total k factor correction is $k = k_{\text{response}} \times k_{\text{inflow}} \times k_{\text{losses}} = 1.30$.

When plotting transverse energy production as a function of centrality, systematic uncertainties are decomposed into three types. Type A uncertainties are point-to-point uncertainties that are uncorrelated between bins and are normally added in quadrature to the statistical uncertainties. However, because there are no Type A uncertainties in this analysis, the vertical error bars represent statistical uncertainties only. Type B uncertainties are bin-correlated such that all points move in the same direction, but not necessarily by the same factor. These are represented by a pair of lines bounding each point. Type C uncertainties are normalization uncertainties in which all points move by the same factor independent of each bin. These are represented as a single error band on the right hand side of each plot. In addition, there is an uncertainty on the estimate of the value of $\langle N_{p0.0art} \rangle$ at each centrality that is represented by horizontal error lines.

There are two contributions to Type B uncertainties, which are added in quadrature to obtain the total Type B uncertainty. The first contribution to Type B uncertainties arises from the uncertainty in the trigger efficiency. The method by which the trigger efficiency is determined is described in [2]. The BBC trigger efficiency is

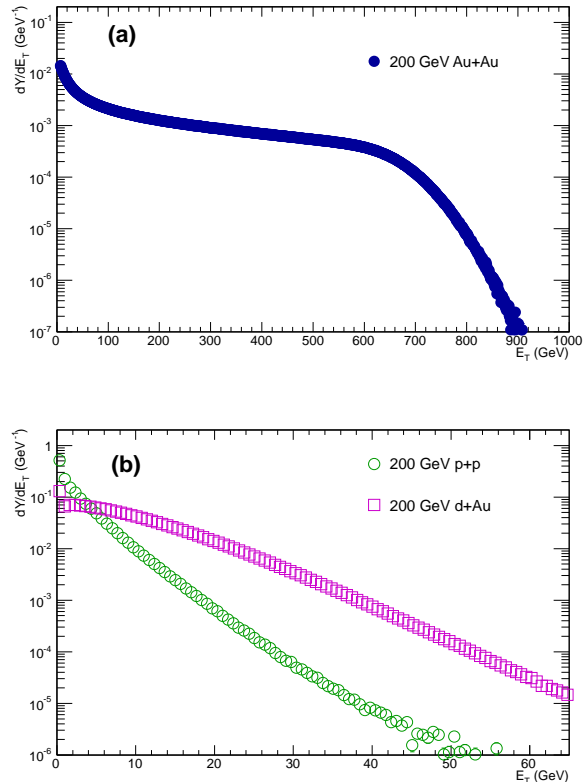


FIG. 3: (Color online) Corrected $E_T = dE_T/d\eta|_{\eta=0}$ distributions at $\sqrt{s_{NN}} = 200$ GeV for 5 sectors of PbSc (a) Au+Au; (b) $p+p$, $d+Au$. The correction factors for each dataset are listed in Table II. All the plots are normalized so that the integral of each distribution is unity.

$92.2\%^{+2.5\%}_{-3.0\%}$ for 200 GeV and 130 GeV Au+Au collisions, $83.7\% \pm 3.2\%$ for 62.4 GeV Au+Au collisions, $88\% \pm 4\%$ for 200 GeV $d+Au$ collisions, and $54.8\% \pm 5.3\%$ for 200 GeV $p+p$ collisions [66]. Because the centrality is defined for a given event as a percentage of the total geometrical cross section, an uncertainty in the trigger efficiency translates into an uncertainty in the centrality definition. This uncertainty is estimated by measuring the variation in $dE_T/d\eta$ by redefining the centrality using trigger efficiencies that vary by ± 1 standard deviation. The second contribution to Type B uncertainties is the uncertainty due to random electronic noise in the EMCAL towers. The noise, or background, contribution is estimated to be consistent with zero with uncertainties tabulated in Table III by measuring the average energy deposited per sector in events where all the particles are screened by the central magnet pole tips by requiring an interaction z -vertex of $+50 < z < +60$ cm and $-50 < z < -60$ cm. A summary of the magnitudes of the Type B uncertainty contributions is listed in Table III.

There are several components to Type C uncertainties, which are also added in quadrature to obtain the total Type C uncertainty. The first contribution is the

uncertainty of the energy response estimate. This uncertainty includes uncertainties in the absolute energy scale, uncertainties in the estimate of the hadronic response, and uncertainties from energy losses on the EM-Cal edges and from energy thresholds. The uncertainties in the hadronic response estimate include a 3% uncertainty estimated using a comparison of the simulated energy deposited by hadrons with different momenta with test beam data [67] along with an additional 1% uncertainty in the particle composition and momentum distribution. Other Type C uncertainties include an uncertainty in the estimate of the EMCal acceptance, an uncertainty in the calculation of the fraction of the total energy incident on the EMCal fiducial area (losses and inflow), and an uncertainty in the centrality determination. A summary of the magnitudes of the Type C uncertainty contributions is listed in Table III. For the MB distributions, the uncertainties on the scale factors previously quoted contain only Type C uncertainties from the energy response, acceptance, and from losses and inflow.

V. ESTIMATING THE NUMBER OF NUCLEON AND QUARK PARTICIPANTS

A Monte-Carlo-Glauber (MC-Glauber) model calculation [68] is used to obtain estimates for the number of nucleon participants at each centrality using the procedure described in [2]. A similar procedure can be used to estimate the number of quark participants, N_{qp} , at each centrality. The quark-quark inelastic cross section for each collision energy is determined such that the inelastic nucleon-nucleon cross section is reproduced. The MC-Glauber calculation is then implemented so that the fundamental interactions are quark-quark rather than nucleon-nucleon collisions. Initially, the nuclei are assembled by distributing the centers of the nucleons according to a Woods-Saxon distribution. Once a nucleus is assembled, three quarks are then distributed around the center of each nucleon. The spatial distribution of the quarks is given by the Fourier transform of the form factor of the proton:

$$\rho^{proton}(r) = \rho_0^{proton} \times e^{-ar}, \quad (4)$$

where $a = \sqrt{12}/r_m = 4.27 \text{ fm}^{-1}$ and $r_m = 0.81 \text{ fm}$ is the rms charge radius of the proton [69]. The coordinates of the two colliding nuclei are shifted relative to each other by the impact parameter. A pair of quarks, one from each nucleus, interact with each other if their distance d in the plane transverse to the beam axis satisfies the condition

$$d < \sqrt{\frac{\sigma_{qq}^{inel}}{\pi}}, \quad (5)$$

where σ_{qq}^{inel} is the inelastic quark-quark cross section, which is varied for the case of nucleon-nucleon collisions

until the known inelastic nucleon-nucleon cross section is reproduced and then used for the A+A calculations. The resulting inelastic quark-quark cross sections are tabulated in Table IV. Figure 4a shows the number of quark participants as a function of the number of nucleon participants. The relationship is nonlinear, especially for low values of N_{part} . Figure 4b shows the resulting ratio of the number of quark participants to the number of nucleon participants as a function of the number of nucleon participants.

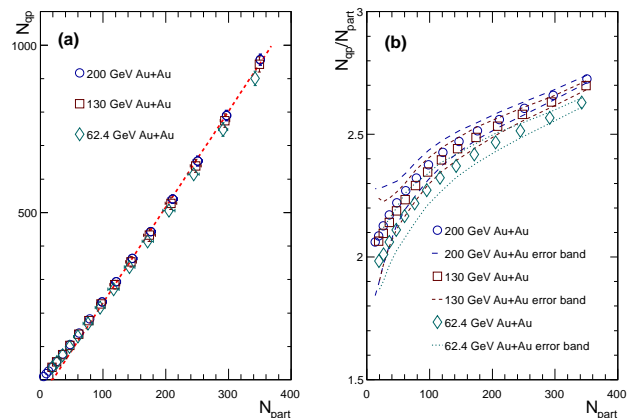


FIG. 4: (Color online) (a) The number of quark participants as a function of the number of nucleon participants. The error bars represent the systematic uncertainty estimate on the MC-Glauber calculation. The dashed line is a linear fit to the 200 GeV Au+Au points with $N_{part} > 100$ to illustrate the nonlinearity of the correlation at low values of N_{part} . (b) The ratio of the number of quark participants to the number of nucleon participants as a function of the number of nucleon participants. The error bands represent the systematic uncertainty estimate on the MC-Glauber calculation.

VI. $dE_T/d\eta$ RESULTS

The distribution of $dE_T/d\eta$ normalized by the number of participant pairs as a function of the number of participants is shown in Figure 5 for Au+Au collisions at $\sqrt{s_{NN}} = 200, 130, \text{ and } 62.4 \text{ GeV}$. The data are also tabulated in Table V for 200 GeV Au+Au, Table VI for 130 GeV Au+Au, and Table VII for 62.4 GeV Au+Au collisions. For all collision energies, the increase seen as a function of N_{part} is nonlinear, showing a saturation towards the more central collisions. However, when $dE_T/d\eta$ is normalized by the number of quark participant pairs, as shown in Figure 6, the data are consistently flat within the systematic uncertainties. Transverse energy production can also be plotted as a function of the number of quark participants as shown in Figure 7. The data for each collision energy are well described by a straight line as shown. The slope parameters for each collision energy are summarized in Table VIII. The consistency with zero of the val-

TABLE III: Summary of the systematic uncertainties given in percent. Listed are uncertainties classified as Type B and Type C. A range is given for Type B uncertainties with the first number corresponds to the most central bin and the second number corresponds to the most peripheral bin.

Error type	System	Au+Au			d+Au	p+p
		200 GeV	130 GeV	62.4 GeV	200 GeV	200 GeV
C	Energy Resp.	3.9%	3.8%	3.9%	3.9%	3.9%
C	Acceptance	3.0%	3.0%	3.0%	3.0%	3.0%
C	Losses and Inflow	3.0%	3.0%	3.0%	3.0%	3.0%
C	Centrality	0.5%	0.5%	0.5%	n/a	n/a
B	Trigger	0.3%-16%	0.3%-16%	0.44%-16%	n/a	n/a
B	Background	0.2%-6.0%	0.4%-10.0%	0.375%-13.3%	6.0%	6.0%

TABLE IV: The inelastic quark-quark cross sections used for each collision energy to reproduce the inelastic nucleon-nucleon cross section.

$\sqrt{s_{NN}}$ (GeV)	$\sigma_{NN}^{\text{inel}}$ (mb)	$\sigma_{qq}^{\text{inel}}$ (mb)
200	42	9.36
130	40	8.60
62.4	35.6	7.08

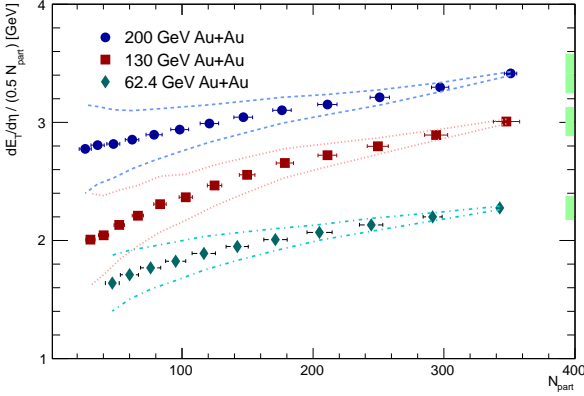


FIG. 5: (Color online) $dE_T/d\eta$ normalized by the number of participant pairs as a function of the number of participants for Au+Au collisions at $\sqrt{s_{NN}} = 200, 130,$ and 62.4 GeV. The Type A uncertainties are represented by error bars about each point. The Type B uncertainties are represented by the lines bounding each point. The Type C uncertainties are represented by the error bands to the right of the most central data point.

ues of the intercept b establish a linear proportionality of E_T with N_{qp} . To summarize, transverse energy production scales *linearly* with the number of constituent-quark participants, in contrast to the nonlinear relationship between transverse energy and the number of participating nucleons.

This nonlinear relationship has been successfully

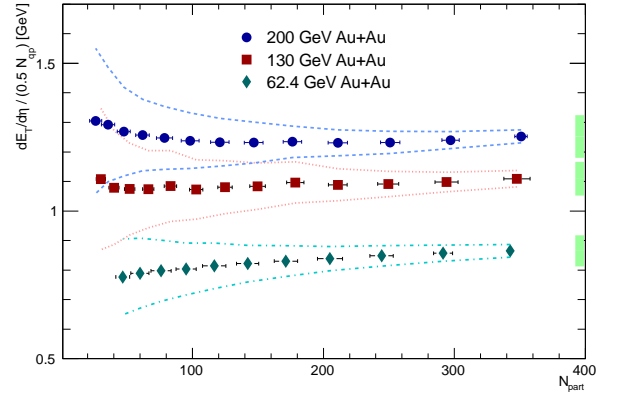


FIG. 6: (Color online) $dE_T/d\eta$ normalized by the number of participant quark pairs as a function of the number of participants for Au+Au collisions at $\sqrt{s_{NN}} = 200, 130,$ and 62.4 GeV. The Type A uncertainties are represented by error bars about each point. The Type B uncertainties are represented by the lines bounding each point. The Type C uncertainties are represented by the error bands to the right of the most central data point.

parametrized as a function of centrality [3, 4, 46]:

$$dE_T^{\text{AA}}/d\eta = (dE_T^{pp}/d\eta) [(1-x)\langle N_{\text{part}} \rangle/2 + x\langle N_{\text{coll}} \rangle], \quad (6)$$

with the implication that the proportionality to N_{coll} is related to a contribution of hard-scattering to N_{ch} and E_T distributions [3, 4]. This seems to contradict the extensive measurements of N_{ch} and E_T distributions in $p+p$ collisions described in Sec. II which show that these distributions represent measurements of the “soft” multi-

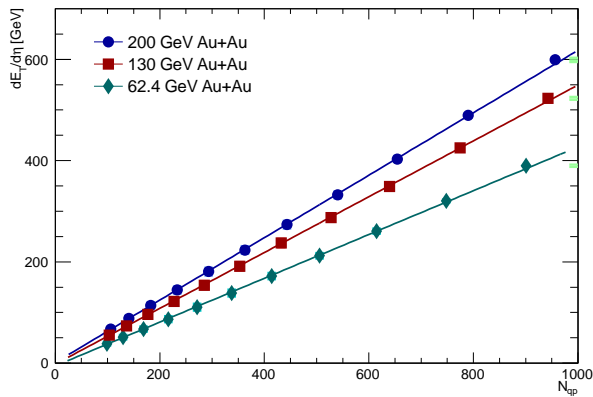


FIG. 7: (Color online) $dE_T/d\eta$ as a function of the number of quark participants for Au+Au collisions at $\sqrt{s_{NN}} = 200, 130,$ and 62.4 GeV. The Type A uncertainties are represented by error bars about each point. The Type B uncertainties are represented by error bands about each point shown. The type A and type B uncertainties are typically less than the size of the data point. The Type C uncertainties are represented by the error bands to the right of the most central data point. The lines are straight line fits to the data.

particle physics that dominates the $p+p$ inelastic cross section. Another argument against a hard-scattering component that the shape of the $dN_{ch}/d\eta/(0.5N_{part})$ vs. N_{part} curves as in Fig. 5 is also the same at 2.76 TeV Pb+Pb collisions [70] although the jet cross section increases by a very large factor. Furthermore, any supposed hard-component in the $p+p$ distributions would be suppressed in A+A collisions [71]. This apparent conflict can be resolved if Eq. 6 is just a proxy for the correct description of the underlying physics, because $dE_T^{AA}/d\eta$ is strictly proportional to N_{qp} (Fig. 7, Table VIII). Using N_{part} , N_{coll} and N_{qp} as a function of centrality, with the value $x = 0.08$ [46, 72], the ansatz in brackets in Eq. 6 is compared to N_{qp} as a function of centrality (Table IX). The striking result is that the ratio $N_{qp}/[(1-x)\langle N_{part} \rangle/2 + x\langle N_{coll} \rangle] = 3.88$ on the average and varies by less than 1% over the entire range except for the most peripheral bin where it drops by 5%. This result demonstrates that rather than implying a hard-scattering component in N_{ch} and E_T distributions, Eq. 6 is instead a proxy for the number of constituent-quark participants N_{qp} as a function of centrality.

It is important to point out that the relationship breaks down more seriously for $p+p$ collisions, with a ratio of 2.99 (Table IX). This is consistent with the PHOBOS [72] result that a fit of Eq. 6 to $\langle dN_{ch}^{AA}/d\eta \rangle$ leaving $\langle dN_{ch}^{pp}/d\eta \rangle$ as a free parameter also projects above the $p+p$ measurement. Because the key to the utility of Extreme Independent Models is that the $p+p$ data, together with an independent calculation of the nuclear geometry can be used to predict the A+A distributions, we now turn to the analysis of the $p+p$, $d+Au$ and Au+Au E_T

distributions at $\sqrt{s_{NN}} = 200$ GeV in terms of these models to see whether the extrapolation from the $p+p$ data using constituent-quark participants is more robust than from the ansatz.

VII. EXTREME-INDEPENDENT ANALYSES IN GENERAL

In Extreme Independent models for an $A+B$ nucleus-nucleus reaction, the nuclear geometry, i.e. the relative probability of the assumed fundamental elements of particle production, such as number of binary nucleon-nucleon (N+N) collisions (N_{coll}), nucleon participants or wounded nucleons (N_{part}, WN), constituent-quark participants (NQP), or color-strings (wounded projectile quarks - AQM), can be computed from the assumptions of the model in a standard Glauber Monte Carlo calculation [68] without reference to either the detector [73] or the particle production by the fundamental elements. Once the nuclear geometry is specified in this manner, it can be applied to the measured $p+p$ distribution (assumed equivalent to N+N) to derive the distribution (in the actual detector) of E_T or multiplicity (or other additive quantity) for the fundamental elementary collision process, i.e. a collision, a wounded nucleon (nucleon participant), constituent-quark participant or a wounded projectile quark (color-string), which is then used as the basis of the analysis of an $A+B$ reaction as the result of multiple independent elementary collision processes. The key experimental issue then becomes the linearity of the detector response to multiple collisions (better than 1% in the present case), and the stability of the response for the different $A+B$ combinations and run periods used in the analysis. The acceptance of the detector is taken into account by making a correction for the probability, p_0 , of measuring zero E_T for an N+N inelastic collision, which can usually be determined from the data [73] (as shown below).

The method for the calculation of the E_T distribution from an $A+B$ reaction in a given detector is illustrated for the N_{coll} or number of binary N+N collision model. The E_T distribution is equal to the sum:

$$\left(\frac{d\sigma}{dE_T}\right)_{N_{coll}} = \sigma_{BA} \sum_{n=1}^{N_{max}} w_n P_n(E_T) \quad (7)$$

where σ_{BA} is the measured $A+B$ cross section in the detector, w_n is the relative probability for n N+N collisions in the $A+B$ reaction with maximum value $n = N_{max}$, and $P_n(E_T)$ is the calculated E_T distribution on the detector for n independent N+N collisions. If $f_1(E_T)$ is the measured E_T spectrum on the detector for an N+N collision that gives a nonzero E_T , and p_0 is the probability for an N+N collision to produce no signal in the detector (zero E_T), then the correctly normalized E_T distribution for one N+N collision is:

$$P_1(E_T) = (1 - p_0)f_1(E_T) + p_0\delta(E_T), \quad (8)$$

TABLE V: Transverse energy production results for 200 GeV Au+Au collisions. Listed are the total uncertainties (Type A, Type B, and Type C) for each centrality bin.

Centrality	$\langle N_{\text{part}} \rangle$	$\langle N_{qp} \rangle$	$\frac{dE_T}{d\eta}$ [GeV]	$\frac{1}{0.5\langle N_{\text{part}} \rangle} \frac{dE_T}{d\eta}$ [GeV]	$\frac{1}{0.5\langle N_{qp} \rangle} \frac{dE_T}{d\eta}$ [GeV]
0%–5%	350.9 ± 4.7	956.6 ± 16.2	599.0 ± 34.7	3.41 ± 0.20	1.25 ± 0.08
5%–10%	297.0 ± 6.6	789.8 ± 15.3	489.7 ± 28.9	3.29 ± 0.19	1.24 ± 0.08
10%–15%	251.0 ± 7.3	654.2 ± 14.5	403.0 ± 25.0	3.21 ± 0.19	1.23 ± 0.08
15%–20%	211.0 ± 7.3	540.2 ± 12.3	332.5 ± 21.2	3.15 ± 0.20	1.23 ± 0.08
20%–25%	176.3 ± 7.0	443.3 ± 10.4	273.6 ± 18.6	3.10 ± 0.21	1.23 ± 0.09
25%–30%	146.8 ± 7.1	362.8 ± 12.2	223.4 ± 16.4	3.04 ± 0.22	1.23 ± 0.09
30%–35%	120.9 ± 7.0	293.3 ± 11.0	180.8 ± 14.3	2.99 ± 0.23	1.23 ± 0.10
35%–40%	98.3 ± 6.8	233.5 ± 9.2	144.5 ± 12.6	2.94 ± 0.25	1.24 ± 0.11
40%–45%	78.7 ± 6.1	182.7 ± 6.8	113.9 ± 10.9	2.90 ± 0.27	1.25 ± 0.12
45%–50%	61.9 ± 5.2	140.5 ± 5.3	88.3 ± 9.3	2.85 ± 0.29	1.26 ± 0.14
50%–55%	47.6 ± 4.9	105.7 ± 5.5	67.1 ± 8.1	2.82 ± 0.33	1.27 ± 0.15
55%–60%	35.6 ± 5.1	77.3 ± 6.8	50.0 ± 6.7	2.81 ± 0.36	1.29 ± 0.17
60%–65%	26.1 ± 4.7	55.5 ± 7.1	36.2 ± 5.4	2.77 ± 0.40	1.30 ± 0.20

TABLE VI: Transverse energy production results for 130 GeV Au+Au collisions. Listed are the total uncertainties (Type A, Type B, and Type C) for each centrality bin.

Centrality	$\langle N_{\text{part}} \rangle$	$\langle N_{qp} \rangle$	$\frac{dE_T}{d\eta}$ [GeV]	$\frac{1}{0.5\langle N_{\text{part}} \rangle} \frac{dE_T}{d\eta}$ [GeV]	$\frac{1}{0.5\langle N_{qp} \rangle} \frac{dE_T}{d\eta}$ [GeV]
0%–5%	347.7 ± 10.0	942.6 ± 22.6	522.8 ± 27.7	3.01 ± 0.16	1.11 ± 0.06
5%–10%	294.0 ± 8.9	774.7 ± 20.3	425.2 ± 23.3	2.89 ± 0.16	1.10 ± 0.07
10%–15%	249.5 ± 8.0	639.6 ± 19.4	349.0 ± 20.3	2.80 ± 0.16	1.09 ± 0.07
15%–20%	211.0 ± 7.2	527.7 ± 18.3	287.2 ± 18.3	2.72 ± 0.17	1.09 ± 0.08
20%–25%	178.6 ± 6.6	432.5 ± 19.0	237.1 ± 16.6	2.66 ± 0.19	1.10 ± 0.09
25%–30%	149.7 ± 6.0	353.0 ± 15.9	191.3 ± 14.9	2.56 ± 0.20	1.08 ± 0.10
30%–35%	124.8 ± 5.5	284.9 ± 13.2	153.9 ± 13.3	2.47 ± 0.22	1.08 ± 0.11
35%–40%	102.9 ± 5.1	227.1 ± 11.0	121.8 ± 11.7	2.37 ± 0.23	1.07 ± 0.12
40%–45%	83.2 ± 4.7	177.1 ± 8.8	96.0 ± 10.8	2.31 ± 0.27	1.08 ± 0.13
45%–50%	66.3 ± 4.3	136.5 ± 7.1	73.3 ± 8.9	2.21 ± 0.28	1.07 ± 0.14
50%–55%	52.1 ± 4.0	103.3 ± 6.5	55.5 ± 7.8	2.13 ± 0.32	1.07 ± 0.16
55%–60%	40.1 ± 3.8	76.0 ± 7.3	41.0 ± 6.6	2.04 ± 0.35	1.08 ± 0.20
60%–65%	30.1 ± 3.6	54.5 ± 7.1	30.2 ± 5.5	2.01 ± 0.40	1.11 ± 0.25

where $\delta(E_T)$ is the Dirac delta function and $\int f_1(E_T) dE_T = 1$. $P_n(E_T)$ (including the p_0 effect) is obtained by convoluting $P_1(E_T)$ with itself $n - 1$ times

$$P_n(E_T) = \sum_{i=0}^n \frac{n!}{(n-i)! i!} p_0^{n-i} (1-p_0)^i f_i(E_T) \quad (9)$$

where $f_0(E_T) \equiv \delta(E_T)$ and $f_i(E_T)$ is the i -th convolution of $f_1(E_T)$:

$$f_i(x) = \int_0^x dy f_1(y) f_{i-1}(x-y) \quad (10)$$

Substituting Eq. 9 into Eq. 7 and reversing the indices gives a form that is less physically transparent, but con-

siderably easier to compute:

$$\left(\frac{d\sigma}{dE_T} \right)_{N_{\text{coll}}} = \sigma_{BA} \sum_{i=1}^{N_{\text{max}}} w'_i(p_0) f_i(E_T) \quad (11)$$

where

$$w'_i(p_0) = (1-p_0)^i \sum_{n=i}^{N_{\text{max}}} \frac{n!}{(n-i)! i!} p_0^{n-i} w_n, \quad (12)$$

which represents the weight (or relative probability) for i convolutions of the measured $f_1(E_T)$ to contribute to the E_T spectrum in an $A+B$ collision, and where the term with $w'_{i=0}(p_0)$ in Eq. 11 is left out because it represents the case when no signal is observed in the detector for an $A+B$ collision, i.e. $w'_{i=0}(p_0) = p_0^{BA}$. Note that

TABLE VII: Transverse energy production results for 62.4 GeV Au+Au collisions. Listed are the total uncertainties (Type A, Type B, and Type C) for each centrality bin.

Centrality	$\langle N_{\text{part}} \rangle$	$\langle N_{qp} \rangle$	$\frac{dE_T}{d\eta}$ [GeV]	$\frac{1}{0.5\langle N_{\text{part}} \rangle} \frac{dE_T}{d\eta}$ [GeV]	$\frac{1}{0.5\langle N_{qp} \rangle} \frac{dE_T}{d\eta}$ [GeV]
0%–5%	342.6 ± 4.9	900.9 ± 21.7	389.7 ± 25.9	2.27 ± 0.13	0.87 ± 0.06
5%–10%	291.3 ± 7.3	748.0 ± 20.4	320.5 ± 21.9	2.20 ± 0.13	0.86 ± 0.06
10%–15%	244.5 ± 8.9	614.7 ± 17.9	260.6 ± 18.8	2.13 ± 0.13	0.85 ± 0.07
15%–20%	205.0 ± 9.6	505.8 ± 16.9	212.1 ± 15.9	2.07 ± 0.13	0.84 ± 0.07
20%–25%	171.3 ± 8.9	414.3 ± 15.2	171.9 ± 14.4	2.01 ± 0.15	0.83 ± 0.08
25%–30%	142.2 ± 8.5	337.2 ± 12.5	138.6 ± 12.9	1.95 ± 0.16	0.82 ± 0.08
30%–35%	116.7 ± 8.9	271.1 ± 12.8	110.4 ± 11.7	1.89 ± 0.18	0.81 ± 0.09
35%–40%	95.2 ± 7.7	216.3 ± 11.0	86.9 ± 10.2	1.83 ± 0.19	0.80 ± 0.10
40%–45%	76.1 ± 7.7	168.8 ± 11.3	67.3 ± 8.7	1.77 ± 0.21	0.80 ± 0.12
45%–50%	59.9 ± 6.9	129.8 ± 9.7	51.2 ± 7.5	1.71 ± 0.23	0.79 ± 0.13
50%–55%	46.8 ± 5.2	98.8 ± 6.1	38.4 ± 6.4	1.64 ± 0.25	0.78 ± 0.14

TABLE VIII: The slope parameters from a linear fit of $dE_T/d\eta$ as a function of N_{qp} , $dE_T/d\eta = a \times N_{qp} + b$ for each collision energy in Au+Au collisions. The value of χ^2 has been calculated including Type A, Type B, and Type C uncertainties for each point.

$\sqrt{s_{NN}}$ (GeV)	a (GeV)	b (GeV)	χ^2	n_{dof}
200	0.617 ± 0.023	1.2 ± 7.0	0.098	9
130	0.551 ± 0.020	-2.1 ± 6.5	0.086	9
62.4	0.432 ± 0.019	-5.4 ± 5.4	0.163	9

the above example works for any other basic element of particle production e.g. constituent-quark-participant, if the labels NQP are substituted above for “ N_{coll} ” and “N+N collision”. The method of determining $p_{0\text{NQP}}$ and $f_1^{\text{NQP}}(E_T)$ will be described below.

In general the convolutions of $f_1(E_T)$ are performed analytically by fitting $f_1(E_T)$ to a Gamma distribution

$$f_1(x) = \frac{b}{\Gamma(p)} (bx)^{p-1} e^{-bx}, \quad (13)$$

where

$$p > 0, \quad b > 0, \quad 0 \leq x \leq \infty,$$

$\Gamma(p)$ is the Gamma function, which equals $(p-1)!$ if p is an integer, and $\int_0^\infty f_1(x) dx = 1$. The first few moments of the distribution are:

$$\mu \equiv \langle x \rangle = \frac{p}{b} \quad \sigma = \frac{\sqrt{p}}{b} \quad \frac{\sigma^2}{\mu^2} = \frac{1}{p}$$

. There are two reasons for this. In general the shape of E_T distributions in $p+p$ collisions is well represented by the Gamma distribution and the n -fold convolution (Eq. 10) is analytical

$$f_n(x) = \frac{b}{\Gamma(np)} (bx)^{np-1} e^{-bx}, \quad (14)$$

i.e. $p \rightarrow np$ while b remains unchanged. Notice that the mean μ_n and standard deviation σ_n of the n -fold

convolution obey the familiar rule:

$$\mu_n = n\mu, \quad \sigma_n = \sigma\sqrt{n}. \quad (15)$$

A. The importance of collisions which give zero measured E_T

The importance of taking account of p_0 , the probability to give zero signal on the detector for an inelastic N+N collision (or other basic element of the calculation) can not be overemphasized. The properly normalized E_T distribution on the detector for one N+N collision is given by Eq. 8, and the detected signal for n independent N+N collisions is given by the binomial distribution, Eq. 9. The true detected mean for n independent N+N collisions is n times the true mean for one N+N collision, or:

$$\langle E_T \rangle_n^{\text{true}} = \int E_T P_n(E_T) dE_T = n \langle E_T \rangle^{\text{true}}, \quad (16)$$

where

$$\begin{aligned} \langle E_T \rangle^{\text{true}} &= \int E_T P_1(E_T) dE_T \\ &= (1 - p_0) \int E_T f_1(E_T) dE_T \\ &= (1 - p_0) \langle E_T \rangle^{\text{ref}}, \end{aligned} \quad (17)$$

TABLE IX: Test of whether the ansatz, $[(1-x)\langle N_{\text{part}}\rangle/2 + x\langle N_{\text{coll}}\rangle]$, from Eq. 6, with $x = 0.08$, is a proxy for N_{qp} . The errors quoted on $\langle N_{\text{part}}\rangle$, $\langle N_{qp}\rangle$, $\langle N_{\text{coll}}\rangle$ are correlated Type C and largely cancel in the $\langle N_{qp}\rangle/\text{ansatz}$ ratio.

Centrality	$\langle N_{\text{part}}\rangle$	$\langle N_{qp}\rangle$	$\langle N_{\text{coll}}\rangle$	ansatz	$\langle N_{qp}\rangle/\text{ansatz}$
0%–5%	350.9 ± 4.7	956.6 ± 16.2	1064.1 ± 110.0	246.5	3.88
5%–10%	297.0 ± 6.6	789.8 ± 15.3	838.0 ± 87.2	203.7	3.88
10%–15%	251.0 ± 7.3	654.2 ± 14.5	661.1 ± 68.5	168.3	3.89
15%–20%	211.0 ± 7.3	540.2 ± 12.3	519.1 ± 53.7	138.6	3.90
20%–25%	176.3 ± 7.0	443.3 ± 10.4	402.6 ± 39.5	113.3	3.91
25%–30%	146.8 ± 7.1	362.8 ± 12.2	311.9 ± 31.8	92.5	3.92
30%–35%	120.9 ± 7.0	293.3 ± 11.0	237.8 ± 24.2	74.6	3.93
35%–40%	98.3 ± 6.8	233.5 ± 9.2	177.3 ± 18.3	59.4	3.93
40%–45%	78.7 ± 6.1	182.7 ± 6.8	129.6 ± 12.6	46.6	3.92
45%–50%	61.9 ± 5.2	140.5 ± 5.3	92.7 ± 9.0	35.9	3.91
50%–55%	47.6 ± 4.9	105.7 ± 5.5	64.4 ± 8.1	27.0	3.91
55%–60%	35.6 ± 5.1	77.3 ± 6.8	43.7 ± 7.6	19.9	3.89
60%–65%	26.1 ± 4.7	55.5 ± 7.1	29.0 ± 6.5	14.3	3.87
65%–70%	18.7 ± 4.0	39.0 ± 6.7	18.8 ± 5.3	10.1	3.86
70%–75%	13.1 ± 3.2	27.0 ± 4.9	12.0 ± 3.6	7.0	3.86
75%–80%	9.4 ± 2.1	19.0 ± 3.2	7.9 ± 2.2	5.0	3.83
80%–92%	5.4 ± 1.2	10.3 ± 1.5	4.0 ± 1.0	2.8	3.67
<i>p+p</i>	2	2.99 ± 0.05	1	1	2.99

and $\langle E_T \rangle^{\text{ref}}$ is the mean of the reference distribution, $f_1(E_T)$, the measured E_T spectrum for an N+N collision that gives nonzero E_T on the detector (Eq. 8). It is important to contrast Eq. 16 with the mean of the n -th convolution of the observed reference distribution, Eq. 10,

$$\begin{aligned} \langle E_T \rangle_n^{\text{ref}} &= \int E_T f_n(E_T) dE_T \\ &= n \langle E_T \rangle^{\text{ref}}, \end{aligned} \quad (18)$$

which is n times the observed reference $\langle E_T \rangle^{\text{ref}}$, as it should be, and which differs from the mean of the true detected distribution, $P_n(E_T)$, for n independently interacting projectile nucleons (Eq. 16) by a factor of $1 - p_0$ for all n , i.e.

$$\begin{aligned} \langle E_T \rangle_n^{\text{true}} &= n \langle E_T \rangle^{\text{true}} \\ &= n(1 - p_0) \langle E_T \rangle^{\text{ref}} = (1 - p_0) \langle E_T \rangle_n^{\text{ref}}. \end{aligned} \quad (19)$$

VIII. APPLICATION TO THE PRESENT DATA

As discussed in section III above, the present measurements at $\sqrt{s_{NN}} = 200$ GeV include Au+Au E_T distributions from the 2004 running period at RHIC and $p+p$ and d +Au distributions from the 2003 run. Although later runs with higher luminosity were tried, they suffer from tails due to pile-up of multiple interactions on the same event, which can be removed with fast electron-

ics,¹ but which was not feasible with the present EMCAL electronics [75]. This is most apparent for the $p+p$ data which is used as the measured E_T distribution, $f_1(E_T)$, for a single N+N collision. The measured E_T distributions, with the requirement of a count ($\text{BBC} \geq 1$) in both the North and South BBC counters, are given as histograms of the number of counts in a given raw $E_{T\text{EMC}}$ bin such that the total number of counts sums up to the number of BBC counts (14,595,815 for $p+p$; 132,884,715 for Au+Au; 50,069,374 for d +Au). The distributions are then normalized to integrate to unity (Fig. 3). Thus the normalized distributions are “per BBC trigger per GeV”, so that the cross section $d\sigma/dE_T$ would be obtained for all distributions by multiplying by the relevant BBC cross section. This is not important for the d +Au or Au+Au data where the normalization is kept as the measured yield per BBC count per GeV in Au+Au or d +Au collisions, but is crucial for the $p+p$ measurement. As discussed previously and tabulated in Table II, the correction scale factors are 6.68 for $p+p$, 6.51 for d +Au and 6.87 for Au+Au, with Type C systematic uncertainties of $\sim \pm 6\%$ which are not relevant for the purposes of this analysis, except as an overall E_T scale uncertainty

¹ For continuous beams, in which fast triggered electronics are used with a short gate width, pile-up can be eliminated by a requirement that no additional interaction take place before or after the interaction of interest in a time interval corresponding to plus or minus the gate width [74]. Of course this requirement reduces the useful luminosity.

common to all 3 distributions to which the absolute scale uncertainty of $\pm 1\%$ must be added. We emphasize that these uncertainties are also common to all the calculations of the $d+Au$ and $Au+Au$ distributions to be presented, because they are based on the measured $p+p$ distribution. Note also that the detailed shape of E_T distributions has a slight dependence on the fiducial aperture due to statistical and dynamical fluctuations which are not taken into account by the simple scale correction. Thus an actual measurement in the reference acceptance will have slightly different upper tails in the region above the “knee” in the $Au+Au$ distribution measured in the fiducial aperture $\Delta\eta \approx 0.7$, $\Delta\phi \approx 0.6\pi$ (Fig. 3a) [76, 77]. Again this is not relevant to the present analysis in which the fiducial aperture is nearly identical for all three systems.

A. Determination of p_0 in the EMCal for an N+N collision

The requirement of the $BBC \geq 1$ trigger complicates the determination of the probability, p_0 , of getting zero energy in the detector, in this case the EMCal, for an inelastic N+N collision, because it introduces a bias. For example, the high point clearly visible in the lowest bin of the $p+p$ data (Fig. 3b) represents the events with zero E_T in the EMCal for a BBC trigger (in addition to the events with nonzero E_T in the lowest bin). This is a necessary quantity to measure but is not the same as p_0 , the probability of getting zero E_T in the EMCal for an inelastic N+N collision. However, the BBC bias can be measured and corrected so that the cross section for E_T production in the EMCal in $p+p$ collisions can be determined; where we assume that $p+p$ and N+N are equivalent for E_T . This is the standard method used for all PHENIX $p+p$ cross section measurements in the EMCal, e.g. π^0 [78] and direct- γ [79], with details of the technique described in these references. The ratio of the measured E_T cross section per $p+p$ collision in the EMCal to the known $p+p$ inelastic cross section, then gives $1 - p_0$ [40].

The $p+p$ data are first fit to a Gamma distribution while expanding the error on the lowest data point by a factor of 10 so that it does not contribute to the fit. The Gamma distribution integrates to a fraction Y_Γ^{pp} of the number of BBC triggers. Then the observed yield per BBC count is converted to the observed cross section by multiplying by the measured BBC cross section of $\sigma_{BBC} = 23.0 \text{ mb} \pm 9.7\%$. This cross section must then be corrected for the BBC bias, $1 - \varepsilon_{bias}$, the probability of getting no BBC count when there is finite energy in the central spectrometer. This was measured using clock triggers for single charged particles in the central spectrometer as well as from the ratio of the yield of high p_T π^0 with and without the $BBC \geq 1$ trigger [79] and found to be a constant $\varepsilon_{bias} = 0.79 \pm 0.02$, independent of p_T . Thus, the measured E_T cross section per $p+p$ collision

equals $Y_\Gamma^{pp} \times \sigma_{BBC} / \varepsilon_{bias}$. The probability of detecting zero E_T in the detector for an inelastic N+N collision is then computed from the ratio of the integrated cross section of the measured E_T distribution to the 42 mb $p+p$ inelastic cross section, σ_{inel} :

$$\begin{aligned} 1 - p_0 &= \frac{1}{\sigma_{inel}} \frac{23.0 \text{ mb} \pm 9.7\%}{0.79 \pm 0.02} Y_\Gamma^{pp} \\ &= 0.693(\pm 10\%) Y_\Gamma^{pp}. \end{aligned} \quad (20)$$

The procedure is a two-step process. First the fit is performed with the error in the lowest bin increased by a factor of 10, so that the counts with zero E_T do not distort the fit. Then trial values of Y_Γ^{pp} and $1 - p_0$ are derived from Eq. 20 and the data are corrected to a data set for which the lowest bin in the distribution is replaced by the fitted value in this bin and the original error is restored, so that the distribution, dY/dE_T which previously integrated to unity, now integrates to Y_Γ^{pp} . This data set is then refit for the final results. The value of $1 - p_0$ is evaluated from the new Y_Γ^{pp} which, with the procedure indicated, typically does not differ significantly from the trial value. The parameters for the fit of the $p+p$ data to a Gamma distribution are given in Table X. Only the data for $E_T < 13.3$ GeV are used in the fit and the following analysis to avoid influence from the tail, which is presumed to be from residual pile-up. However, the fit was also extended to $E_T < 26.6$ GeV as a systematic check (Fig. 8).

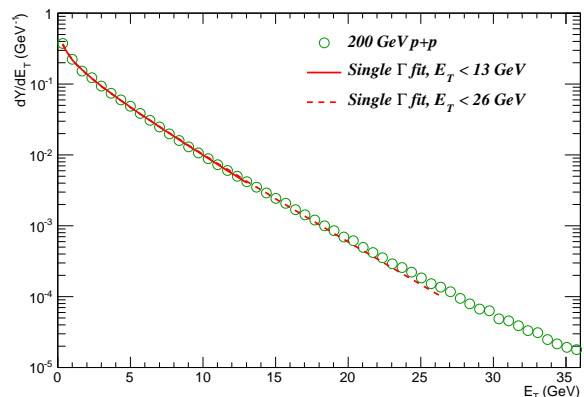


FIG. 8: (Color online) Fits of the $p+p$ data to a single Γ distribution for the ranges $E_T < 13.3$ and $E_T < 26.6$ GeV.

The poor χ^2_{min}/dof for both fits has at least two sources. For low E_T , the statistical uncertainties with millions of events per bin are $\sim 1/1000$ so any uncorrected few percent systematic effect for each data point (e.g. such as not bin-shifting for the falling spectrum) gives a large contribution to the χ^2 . At larger $E_T > 20$ GeV, the data clearly lie above the fit, which is emphasized by the fit with $E_T < 26.6$ GeV. This difference is presumed to be due to residual pile-up. In any case, the

fits for both E_T ranges follow the $p+p$ data for more than two orders of magnitude and have $\langle E_T^{\text{ref}} \rangle$ which differ by 0.6%, so are more than adequate for the multiple collision calculations, for which the dominant effect in convolutions is the mean value. An 0.6% variation in $\langle E_T^{\text{ref}} \rangle$ will result in an 0.6% change in the E_T scale of the calculations which is negligible compared to the dominant systematic uncertainty to be discussed below. The tail only enters when the geometry is exhausted [40], which is not reached for the present $d+Au$ and $Au+Au$ data. Following the standard practice, the uncertainties on the fitted parameters, Y_{Γ}^{pp} , b and p , in Table X have been increased by a factor of $\sqrt{4866/17} = 16.9$ and $\sqrt{6715/37} = 13.4$, respectively. Thus, the fractional statistical uncertainty on $1 - p_0$ from the fitted Y_{Γ}^{pp} is $0.006/0.933 = 0.6\%$, which is still small compared to the uncertainties on the parameters in Eq. 20 of which the 9.7% uncertainty in the BBC cross section is predominant. Adding the 0.6% fractional uncertainty in quadrature with the two fractional uncertainties on the parameters in Eq. 20 gives a total systematic uncertainty on $1 - p_0$ of 10.1%. Thus, the values of $1 - p_0$ are taken as 0.647, 0.660, with a systematic uncertainty of 10% as indicated in Table X.

B. Calculations of the various models

The starting point requires the relative probabilities, w_n , for the number of binary N+N collisions, nucleon participants, constituent-quark participants from q-q scattering (NQP), and wounded projectile quarks from q-N scattering (AQM) for $\sqrt{s_{NN}} = 200$ GeV $p+p$, $d+Au$, $Au+Au$ collisions. These were calculated by the standard Glauber Monte Carlo method, as described in section V. For $Au+Au$ they are plotted in Fig. 9.

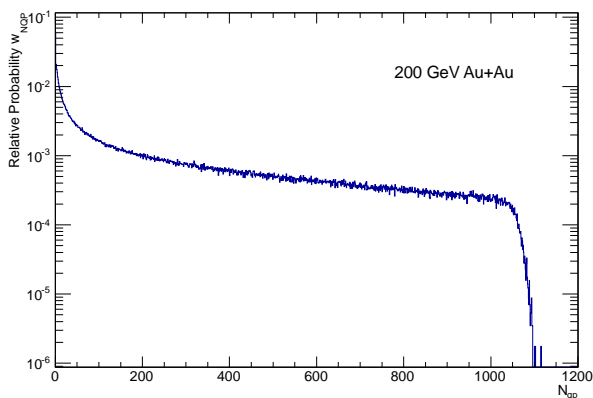


FIG. 9: (Color online) Distribution of the Number of Quark Participants in $Au+Au$ at $\sqrt{s_{NN}} = 200$ GeV

There was no explicit AQM calculation in $Au+Au$; the probability for n wounded projectile quarks was taken to be the sum of the probabilities for $2n$ and $2n - 1$

constituent-quark participants. The weights for $p+p$ and $d+Au$ are tabulated in Tables XI and XII. The weights in these tables are defined as the ‘original’ weights, ($p_0 = 0$, $\epsilon \equiv 1 - p_0 = 1.0$), before correction for p_0 .

1. Correction of the weights w_n to $w'_i(p_0)$ for N_{part} , NQP and AQM in $p+p$ to account for p_0

Because the p_0 is calculated for a $p+p$ collision, one has to recompute the $p+p$ weights in each model to find the $p_{0\text{AQM}}$, $p_{0\text{NQP}}$, and $p_{0\text{Npart}}$ so that the new weights for the elementary processes sum up to $1 - p_0$ for the $p+p$ collision. The value $1 - p_0 = 0.647$ for $p+p$ collisions, from Table X, gives the probability $p_0 = 0.353$ for an inelastic N+N collision to give zero energy into our acceptance, i.e. zero detected $E_{T\text{EMC}}$. For N_{coll} , which is based on N+N collisions, p_0 is simply that of a $p+p$ collision. For N_{part} , because a $p+p$ collision is 2 participants, it is assumed that both participants had equal $p_{0\text{Npart}}$, and so the case when only 1 WN deposited energy is not counted. This is done because both BBCs are required to count on a N+N collision although there are certainly cases when both WN could give a BBC count but only 1 would give a nonzero E_T . If the case when only 1 WN deposited energy were allowed, then the only way to get zero energy on a $p+p$ collision is for both WN to give zero energy i.e. $p_{0\text{WN}} = p_0^2 = 0.125$, $\epsilon_{\text{WN}} = 0.875$, but then the weight for 1 WN would have to be included in this calculation. We chose instead to require both WN to deposit energy, hence a $p+p$ collision equaled 2 WN, i.e. $\epsilon_{pp} = 1 - p_0 = \epsilon_{\text{WN}}^2$, so $\epsilon_{\text{WN}} = \sqrt{1 - p_0} = 0.804$.

For NQP, Eq. 12 was used to calculate the value of $w'_{i=0}(p_{0\text{NQP}})$ for any $p_{0\text{NQP}}$ with the case NQP=1 not allowed, so $w'_{i=0}(p_{0\text{NQP}}) + w'_{i=1}(p_{0\text{NQP}}) = p_0 = 0.353$ was solved, with result $\epsilon_{\text{QP}} = 1 - p_{0\text{NQP}} = 0.659$. For the AQM, the total efficiency of the projectile quarks (color-strings) should add up to the efficiency of a $p+p$ collision at midrapidity. Thus the equation $w'_{i=0}(p_{0\text{AQM}}) = p_0 = 1 - 0.647 = 0.353$ was solved, with result $\epsilon_{\text{AQM}} = 1 - p_{0\text{AQM}} = 0.538$.

Note that there can be confusion in the AQM model because in a $p+p$ collision, represented as 1 to 3 q+p collisions, the struck proton may have the efficiency of a Wounded Nucleon rather than that of a Wounded Projectile Quark. Such an asymmetric AQM model can be calculated. However, if one thinks of the AQM model as the number of color strings rather than number of wounded projectile quarks, then the detection efficiency, $\epsilon_{\text{AQM}} = 1 - p_{0\text{AQM}} = 0.538$, can be thought of as the detection efficiency for a color string.

2. Correcting the $p+p$, $d+Au$ and $Au+Au$ weights.

Applying $p_{0\text{AQM}}$, $p_{0\text{NQP}}$, and $p_{0\text{WN}}$ to correct the $p+p$, $d+Au$ and $Au+Au$ weights is straightforward and given by Eq. 12. The weights from Tables XI and XII corrected

TABLE X: Fitted parameters Y_{Γ}^{pp} , b , p of $p+p$ data, and calculated $1 - p_0$. Note that the standard errors on these parameters using $\chi^2 = \chi_{\min}^2 + 1$ have been multiplied by $\sqrt{\chi_{\min}^2/\text{dof}}$ in each case.

System	Y_{Γ}^{pp}	b (GeV) $^{-1}$	p	$\langle E_T \rangle^{\text{ref}}$ GeV	χ_{\min}^2/dof	$1 - p_0$
$p+p$ $E_T < 13.3$	0.933 ± 0.006	0.273 ± 0.003	0.724 ± 0.010	2.64	4866/17	0.647 ± 0.065
$p+p$ $E_T < 26.6$	0.952 ± 0.004	0.263 ± 0.003	0.692 ± 0.007	2.63	6715/37	0.660 ± 0.066

TABLE XI: Original weights w_n ($p_0 = 0$, $\epsilon \equiv 1 - p_0 = 1.0$) for $p+p$ and $d+Au$ at $\sqrt{s} = 200$ GeV. Note that $\sigma = 9.36$ mb was used for q-q scattering to obtain a N+N $\sigma^{\text{inel}} = 42.0$ mb. These AQM weights come from the q-q scattering calculation tabulated from the distribution of projectile participants, NQP (p), NQP(deuteron). The symbol “...” in the table indicates additional weights for $n \geq 7$.

n	$p+p$		$d+Au$		Au+Au	
	NQP	AQM	NQP	AQM	N_{part}	NQP
1	0.00	0.609	0.00	0.131	0.00	0.00
2	0.465	0.285	0.0867	0.124	0.0660	0.0613
3	0.238	0.106	0.0516	0.202	0.0304	0.0204
4	0.169		0.0529	0.0925	0.0269	0.0209
5	0.0946		0.0473	0.118	0.0220	0.0176
6	0.0333		0.0451	0.332	0.0195	0.0157
7		

TABLE XII: Original N_{coll} and AQM weights w_n ($p_0 = 0$, $\epsilon \equiv 1 - p_0 = 1.0$) for Au+Au at $\sqrt{s} = 200$ GeV. Note that $\sigma = 9.36$ mb was used for q-q scattering to obtain a N+N $\sigma^{\text{inel}} = 42.0$ mb. The symbol “...” in the table indicates additional weights for $n \geq 7$.

n	Au+Au N_{coll}	Au+Au AQM
1	0.0660	0.0613
2	0.0405	0.0414
3	0.0287	0.0333
4	0.0232	0.0263
5	0.0191	0.0214
6	0.0169	0.0184
7

for these efficiencies are summarized in Tables XIII and XIV.

3. Derivation of the E_T distribution of the basic elements from the $p+p$ E_T distributions followed by calculation of the $d+Au$ and $Au+Au$ distributions

At this point the raw $E_{T\text{EMC}}$ distributions in the fiducial aperture had been corrected to the total hadronic $E_T = dE_T/d\eta|_{\eta=0}$ by making a change of scale from $E_{T\text{EMC}}$ to E_T by the correction factors of 6.68 for $p+p$, 6.51 for $d+Au$ and 6.87 for $Au+Au$ (Fig. 3). The $p+p$ and the elementary WN, NQP, AQM distributions $f_i(E_T)$ in Eqs. 8–11 are taken as Γ distributions and then the $p+p$ distribution (Fig. 3b) is deconvoluted using the efficiency corrected weights, w'_i , to find the parameters of the elementary NQP, or AQM distributions. For the WN the deconvolution from $p+p$ is analytical.

The results of the fit to a single Γ distribution ($p+p$) were given in Table X and Fig. 8. The deconvolution of $p+p$ to sums of elementary Γ distributions with AQM and NQP weights w'_i are shown in Fig. 10 and given in Table XV.

These parameters are then used in Eq. 11 with the $d+Au$ and $Au+Au$ corrected weights to compute the E_T distributions for these systems. The results for the Additive Quark Model (AQM) using the above $\epsilon_{\text{AQM}} = 1 - p_{0\text{AQM}} = 0.538$ and the constituent-Quark Participant (NQP) model with $\epsilon_{\text{NQP}} = 1 - p_{0\text{NQP}} = 0.659$ are shown for $Au+Au$ in Fig. 11. Both the shape and magnitude of the calculation with the NQP model are in excellent agreement with the entire $Au+Au$ measurement including the upper edge of the calculation, which is essentially on top of the measured E_T distribution, well within the principal $\pm 10\%$ systematic uncertainty in $1 - p_0$ from the BBC cross section (Eq. 20). This uncertainty is common to both AQM and NQP calculations so does not affect

TABLE XIII: Corrected weights w'_i for $p+p$, $d+Au$ $Au+Au$, at $\sqrt{s} = 200$ GeV. Note that $1 - p_0$ is the sum of the weights in the column (including weights not tabulated) and is the not the BBC efficiency, but the probability to get a nonzero $E_{T\text{EMC}}$ on an $A+B$ collision.

n	$p+p$		$d+Au$		$Au+Au$	
	NQP $\epsilon_{\text{NQP}}=0.659$	AQM $\epsilon_{\text{AQM}}=0.538$	NQP $\epsilon_{\text{NQP}}=0.659$	AQM $\epsilon_{\text{AQM}}=0.538$	N_{part} $\epsilon_{\text{WN}}=0.804$	AQM $\epsilon_{\text{NQP}}=0.659$
1	0.00	0.506	0.00	0.259	0.00	0.00
2	0.378	0.125	0.0918	0.251	0.0596	0.0474
3	0.173	0.0164	0.0726	0.199	0.0333	0.0270
4	0.0731		0.0664	0.120	0.0277	0.0231
5	0.0202		0.0601	0.0467	0.0230	0.0195
6	0.00272		0.0552	0.00802	0.0199	0.0168
7		
$1-p_0$	0.647	0.647	0.926	0.883	0.973	0.956

TABLE XIV: Corrected weights w'_i for $Au+Au$ at $\sqrt{s} = 200$ GeV. Note that $1 - p_0$ is the sum of the weights in the column (including weights not tabulated) and is the not the BBC efficiency, but the probability to get a nonzero $E_{T\text{EMC}}$ on the $A+B$ collision.

n	N_{coll}	AQM
	$\epsilon_{\text{coll}}=0.647$	$\epsilon_{\text{AQM}}=0.538$
1	0.0723	0.0756
2	0.0433	0.0494
3	0.0312	0.0362
4	0.0247	0.0284
5	0.0205	0.0235
6	0.0175	0.0202
7
$1-p_0$	0.970	0.958

TABLE XV: Parameters b , p of the element indicated from the fit to $p+p$ data, cut for $E_T < 13.3$ GeV ($E_{T\text{EMC}} < 2$ GeV). Y_{Γ}^{fit} is the fitted integral of the $p+p$ distribution. For N_{coll} , the fit is a single Γ to the $p+p$ distribution from which ϵ_{pp} is calculated; for N_{part} , $p_{\text{WN}} = p_{pp}/2$, $\epsilon_{\text{WN}} = \sqrt{\epsilon_{pp}}$. For NQP and AQM the fits are the deconvolution of elements with weights w'_i which do not sum to unity but sum to $\epsilon_{pp} = 0.647$ so that $Y_{\Gamma}^{pp} = Y_{\Gamma}^{fit} \times \epsilon_{pp} = 0.948$ (NQP), 0.944 (AQM), a good check (within 1.6% and 1.1% respectively).

Model	$\epsilon_{\text{element}}$	element	Y_{Γ}^{fit}	b (GeV) ⁻¹	p	$\langle E_T \rangle_{\text{elem}}^{\text{ref}}$ (GeV)	$\langle E_T \rangle_{\text{elem}}^{\text{true}}$ (GeV)
N_{coll}	0.647	$p+p$	0.933	1.83/6.68	0.723	2.64	1.71
N_{part}	0.804	1 WN	0.933	1.83/6.68	0.363	1.32	1.06
NQP	0.659	1 QP	1.466	2.00/6.68	0.297	0.994	0.655
AQM	0.538	1 string	1.460	2.10/6.68	0.656	2.09	1.12

the difference in the AQM and NQP curves, both curves scale together in E_T by the same $\pm 10.1\%$ with respect to the data. Another advantage of the Extreme Independent Models is that all the calculations are based on the measured data. Thus the 6% Type C common systematic uncertainty on the absolute E_T scale (Table III) cancels in relative comparisons of the data to the calculations—all the curves and the data scale together by the same fraction in E_T .

Interestingly, the AQM model is not identical to the NQP model for the symmetric $Au+Au$ system, but 12% lower in the E_T knee. This is due to the p_0 effect in the $p+p$ collision, which has different effects on the AQM and NQP calculations. This was checked by repeating the AQM (color-string) and NQP calculations with $1 - p_0 = 1.0$ detection efficiency in a $p+p$ collision to confirm that the AQM and NQP models really do give identical results in symmetric $Au+Au$ collisions for 100% efficiency.

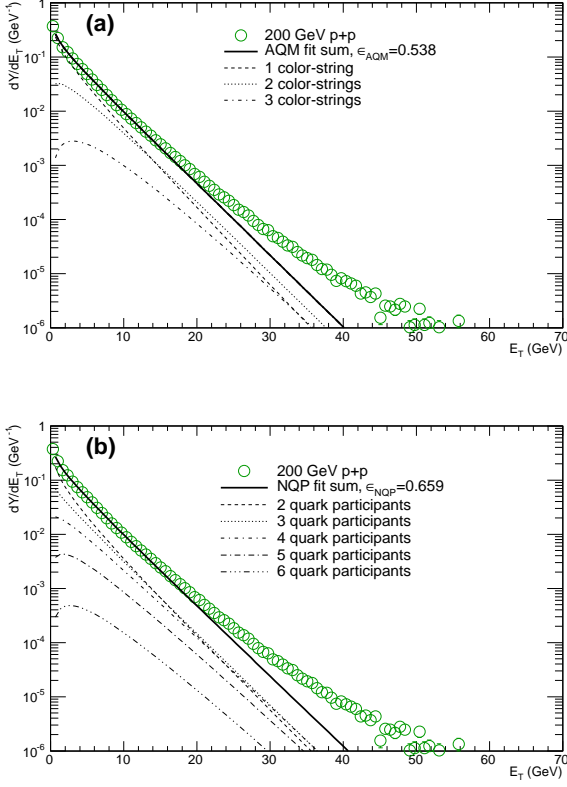


FIG. 10: (Color online) (a) Deconvolution fit to the $p+p$ E_T distribution for $E_T < 13.3$ GeV at $\sqrt{s_{\text{NN}}} = 200$ GeV with the corrected weights w_i^{AQM} calculated in the Additive Quark model (AQM) using the symmetric color-string efficiency, $\epsilon_{\text{AQM}} = 1 - p_{0\text{AQM}} = 0.538$. Lines represent the properly weighted individual E_T distributions for 1, 2, 3 color-strings plus the sum. On the y-axis intercept, the top line is the sum and the lower curves in descending order are the E_T distributions of 1,2,3 color-strings. (b) Deconvolution fit to the same $p+p$ E_T distribution for $E_T < 13.3$ GeV with the corrected weights w_i^{NQP} with $\epsilon_{\text{NQP}} = 1 - p_{0\text{NQP}} = 0.659$ calculated in the NQP model. Lines represent the properly weighted individual E_T distributions for the underlying 2, 3, 4, 5, 6 constituent-quark participants plus the sum.

The major difference in the NQP and AQM calculations with respect to the measurements shows up in the asymmetric $d+\text{Au}$ system, Fig. 12, where the NQP calculation closely follows the $d+\text{Au}$ E_T distribution in shape and in magnitude over a range of a factor of 1000 in cross section. The AQM calculation disagrees both in shape and magnitude, with a factor of 1.7 less transverse energy emission than in the measurement. This clearly indicates the need for emission from additional quark participants in the Au target beyond those in the deuteron, as shown by the individual components of the NQP calculation for $d+\text{Au}$ (Fig. 13). It is also clear that having the comparison between the NQP and AQM models for asymmetric systems is crucial in distinguishing the models.

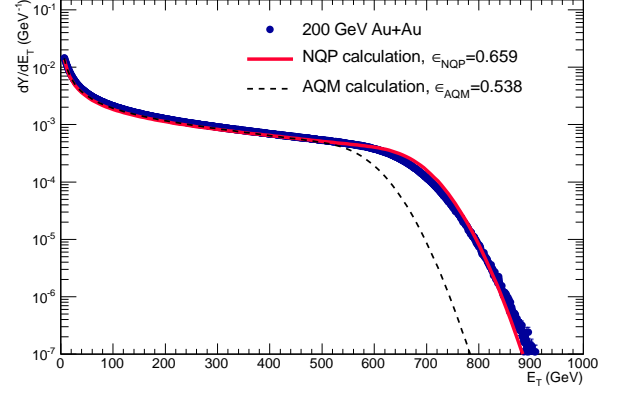


FIG. 11: (Color online) E_T distributions at $\sqrt{s_{\text{NN}}} = 200$ GeV calculated in the Number of constituent-Quark Participants or NQP model, with $\epsilon_{\text{NQP}} = 1 - p_{0\text{NQP}} = 0.659$ for Au+Au together with the AQM calculations with efficiencies indicated.

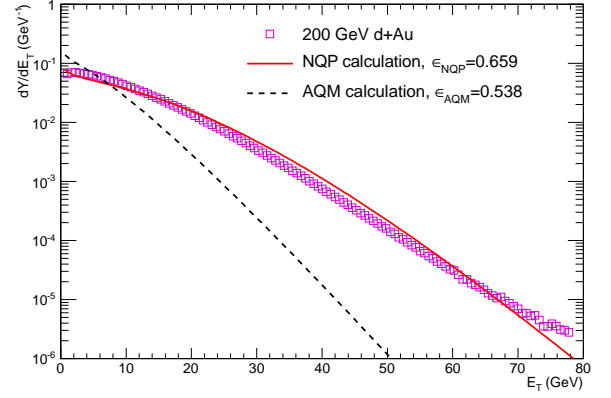


FIG. 12: (Color online) $d+\text{Au}$ measurements compared to the AQM and NQP model calculations.

Previously, the hypothesis of quark-participant scaling in Au+Au collisions had been tested only for mean values by plotting $\langle dE_T/d\eta \rangle / (\langle N_{qp} \rangle / 2)$ vs N_{part} [5, 47, 48] as applied here in Fig. 6. The present work extends the NQP model to *distributions*, as described in section VIII and shown in Fig. 11. By doing so, we are able to make a crucial consistency check—the $\langle dE_T/d\eta \rangle / N_{qp} = 0.617 \pm 0.023$ GeV from the linear fit (Fig. 7) in Au+Au is equal (within < 1 standard deviation) to the value $\langle E_T \rangle_{qp}^{\text{true}} = 0.655 \pm 0.066$ GeV derived for a quark-participant from the deconvolution of the $p+p$ E_T distribution (Table XV).

C. Additional Systematic Uncertainties

The probability p_0 of detecting zero E_T in the central detector for an N+N or other elementary collision plays a major role in this analysis. The predominant systematic

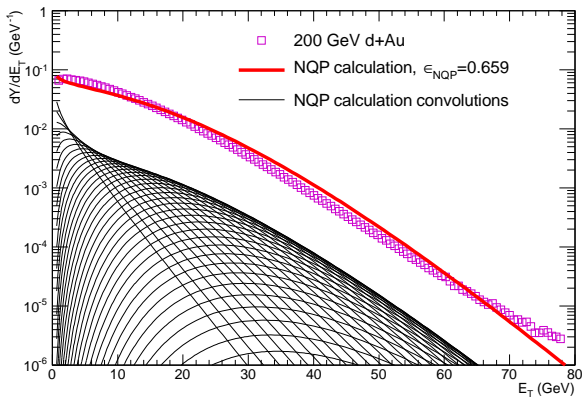


FIG. 13: (Color online) E_T distributions at $\sqrt{s_{NN}} = 200$ GeV in $d+Au$ calculated in the Quark Participant (NQP) model with $\epsilon_{\text{NQP}} = 1 - p_{0\text{NQP}} = 0.659$ together with the individual visible convolutions for NQP, i.e. 2,3,...33, out of a maximum of 50 NQP considered.

uncertainty comes from the BBC cross section measurement (Eq. 20) which leads to a total systematic uncertainty on $1 - p_0$ of 10.1% for a $p+p$ collision as indicated in Table X. The systematic uncertainty is propagated by varying $1 - p_0$ from 0.647 to 0.712 and 0.582, ± 1 standard deviation, from Eq. 20 for standard $E_{T\text{EMC}} < 2$ GeV ($E_T < 13.3$ GeV) $p+p$ data and repeating all the calculations (to be shown in Sec. IX). Also all the fits were redone with the $E_{T\text{EMC}} < 4$ GeV ($E_T < 26.6$ GeV) $p+p$ data, and the calculations were again all repeated, with a small effect (Fig. 14).

Another important issue must be mentioned in the comparison of the calculations to the measurements. The calculations are per $A+B$ collision (corrected for BBC efficiency) while the data are per BBC count and are not corrected for the BBC efficiency. This correction is complicated for both $d+Au$ and $Au+Au$, but larger for $Au+Au$ due to the more severe BBC requirement. To get an idea of the size of the effect, Fig. 15 shows the $Au+Au$ data and the NQP calculation of Fig. 11 on the same E_T scale as in $d+Au$ collisions (see Fig. 13). The inefficiency in the data compared to the $Au+Au$ calculation is negligible for $E_T \geq 7$ GeV, as shown, which should be less severe for $d+Au$ and therefore does not affect the conclusion from Fig. 12 that rejects the AQM model in favor of the NQP model.

IX. FINAL RESULTS AND DISCUSSION

The principal results were given in Figs. 11 and 12. The final results are now presented in Fig. 16 including the systematic uncertainties. In Fig. 16a, the $Au+Au$ $E_T \equiv dE_T/d\eta|_{y=0}$ distribution is shown compared to the NQP calculations using the central $1 - p_0 = 0.647$ and $\pm 1\sigma$ variations of $1 - p_0 = 0.582, 0.712$ for the proba-

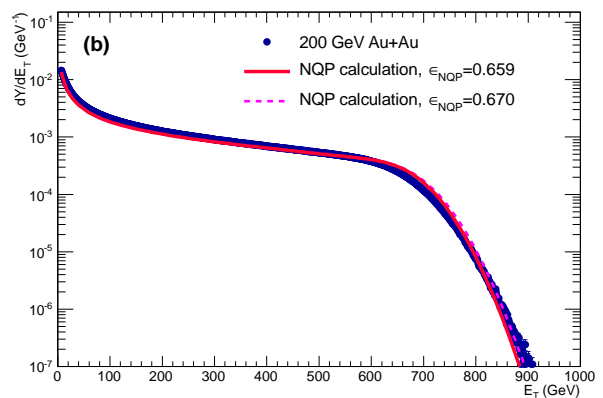
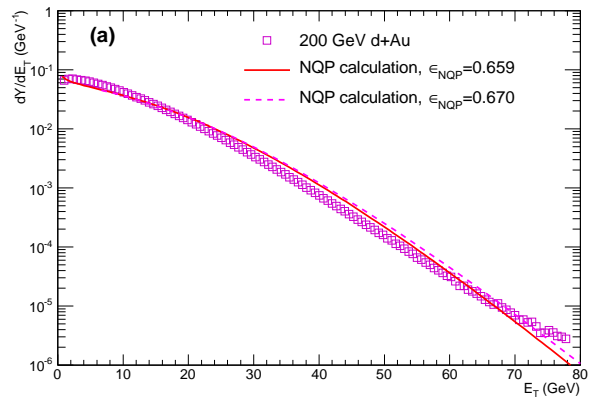


FIG. 14: (Color online) Systematic checks of $E_T \equiv dE_T/d\eta|_{y=0}$ calculations using $p+p$ fits with $E_T < 26.6$ GeV (a) $d+Au$ data compared to standard calculation in the NQP model with $\epsilon_{\text{NQP}} = 1 - p_{0\text{NQP}} = 0.659$, for $1 - p_0 = 0.647$ in a $p+p$ collision from fit with $E_T < 13.3$ GeV compared to $\epsilon_{\text{NQP}} = 1 - p_{0\text{NQP}} = 0.670$ for $1 - p_0 = 0.660$ when the fit to the $p+p$ data is extended to $E_T < 26.6$ GeV. (b) $Au+Au$ calculation for the same conditions as $d+Au$ in (a).

bility of getting zero E_T on a $p+p$ collision, which correspond to $\epsilon_{\text{NQP}} = 0.659, 0.603, 0.716$ respectively. Both the shape and magnitude of the calculation with the NQP model are in excellent agreement with the $Au+Au$ measurement. The upper edge of the calculation using the central $1 - p_0$ is essentially on top of the measured E_T distribution, well within the principal $\pm 10\%$ systematic uncertainty shown, while the AQM model (recall Fig. 11) was another 12% lower due to the nonzero p_0 in $p+p$ collisions in this measurement which leads to different efficiencies of a quark participant and a color string.

In Fig. 16b the $d+Au$ E_T distribution is shown with the central $1 - p_{0\text{NQP}}$ and the $\pm 1\sigma$ variations. The NQP calculation closely follows the $d+Au$ measurement in shape and in magnitude over a range of a factor of 1000 in cross section, while as previously seen in Fig. 12, the AQM calculation disagrees both in shape and magnitude, with nearly a factor of 2 less E_T emission. A new independent check of the NQP model is the observation that the

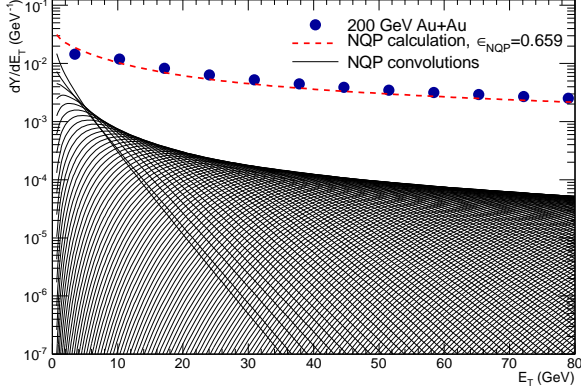


FIG. 15: (Color online) Measured E_T distribution in Au+Au at $\sqrt{s_{NN}} = 200$ GeV on the same E_T scale as Fig. 13 compared to the calculation in the Quark Participant (NQP) model with $\epsilon_{NQP} = 1 - p_{0NQP} = 0.659$ together with the individual visible convolutions for NQP in this E_T range, i.e. 2,3, ... 114, out of 584 convolutions with visible contribution to the full distribution, out of a maximum of 1020 NQP considered.

$\langle dE_T/d\eta \rangle / N_{qp} = 0.617 \pm 0.023$ GeV calculated from the linear fit (Fig. 7) of the Au+Au measurement as a function of centrality is equal (within < 1 standard deviation) to the value $\langle E_T \rangle_{qp}^{\text{true}} = 0.655 \pm 0.066$ GeV derived for a quark-participant from the deconvolution of the $p+p$ E_T distribution (Table XV).

The availability of the $p+p$ baseline E_T distribution together with the Au+Au distribution allows a test of how the representation of $dN_{ch}/d\eta$ or $dE_T/d\eta$ as a function of centrality by this rewrite of Eq. 6 [3, 4, 46]:

$$dE_T^{AA}/d\eta = [(1-x)\langle N_{\text{part}} \rangle (dE_T^{pp}/d\eta)/2 + x\langle N_{\text{coll}} \rangle (dE_T^{pp}/d\eta)], \quad (21)$$

which works for the average values, could be applied to the distributions.

Figure 17 compares the Au+Au data to the N_{coll} and N_{part} -WNM calculations, including the efficiencies. One thing that is immediately evident from Fig. 17 is that if Eq. 6,21 were taken to represent the weighted sum of $(1-x) \times$ the WNM- N_{part} curve + $x \times$ the N_{coll} curve with $x \approx 0.08$ [46, 72], then the representation of $dE_T/d\eta$ by Eq. 6,21, which may seem reasonable for the average values, makes no sense for the distribution.

To further emphasize this point, shown in Fig. 18 is the calculation of the distribution given by Eq. 6,21 for 10%–15% centrality, namely the sum of the N_{part} distribution for $\langle N_{\text{part}} \rangle = 254$, weighted by $(1-x)$, and the N_{coll} distribution for $\langle N_{\text{coll}} \rangle = 672$ weighted by x , compared to the measured Au+Au distribution for 10%–15% percentile centrality region.² Although it is reasonable that the

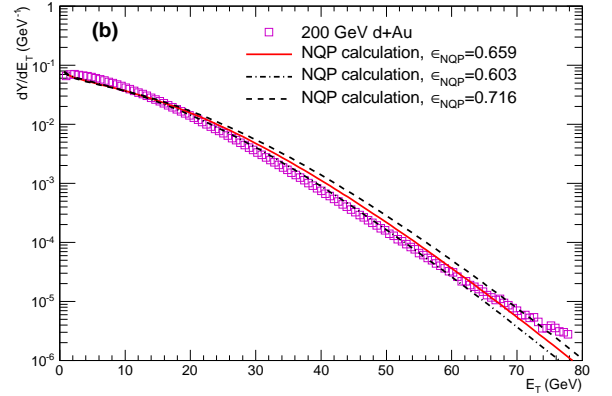
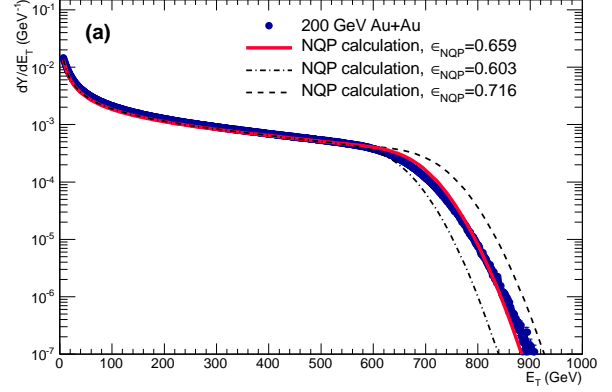


FIG. 16: (Color online) $E_T \equiv dE_T/d\eta|_{y=0}$ distributions at $\sqrt{s_{NN}} = 200$ GeV: (a) Au+Au compared to the NQP calculations using the central $1 - p_0 = 0.647$ and $\pm 1\sigma$ variations of $1 - p_0 = 0.582, 0.712$ for the probability of getting zero E_T on a $p+p$ collision with resulting $\epsilon_{NQP} = 0.659, 0.603, 0.716$, respectively. (b) $d+Au$ calculation for the same conditions as in (a).

weighted sum of the averages of the N_{coll} and N_{part} distributions could equal the average of the measured $dE_T/d\eta$ distribution for 10%–15% centrality, the weighted sum of the actual N_{coll} and N_{part} distributions would look totally unreasonable and nothing like the measured $dE_T/d\eta$ distribution cut on centrality. Thus Eq. 6 can not be interpreted as the weighted sum of the N_{coll} and N_{part} distributions. Furthermore, as shown in Fig. 19, neither can Eq. 6 be interpreted as the sum of the N_{coll} and N_{part} distributions scaled in E_T by the factors x and $1-x$ respectively. Hence it does not seem that Eq. 6 can be computed in an extreme independent model.

Recent experiments at the Large Hadron Collider, the ATLAS experiment in particular [80], have shown that

² The curves in Fig. 18 are actually for $254 \times (\epsilon_{N_{\text{part}}} = 0.804) =$

204 convolutions of $f_1^{N_{\text{part}}}$ and $672 \times (\epsilon_{N_{\text{coll}}} = 0.647) = 435$ convolutions of the $p+p$ measured reference distribution, $f_1^{N_{\text{coll}}}(E_T)$ following Eq. 20.

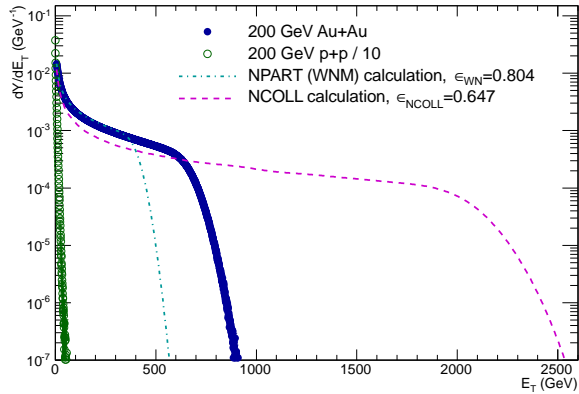


FIG. 17: (Color online) Au+Au measurement of $dE_T/d\eta$ compared to the N_{part} -WNM (dot-dash) and N_{coll} (dashes) model calculations.

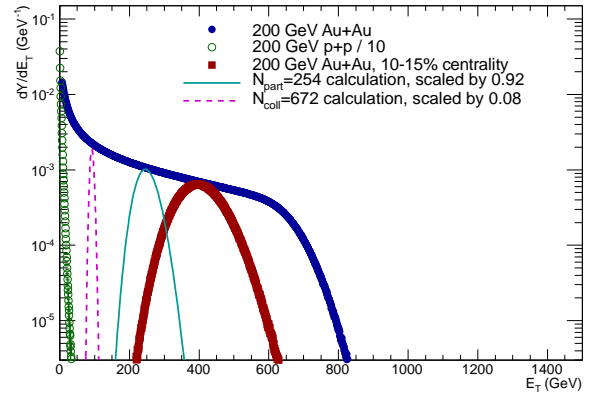


FIG. 19: (Color online) Au+Au measurement of $dE_T/d\eta$, with 10%–15% centrality region indicated, compared to the calculation of the distribution given by Eq. 21 for $N_{\text{part}}=254$ and $N_{\text{coll}}=672$ corresponding to 10%–15% centrality, where the distributions have been scaled in E_T by 0.92 and 0.08, respectively.

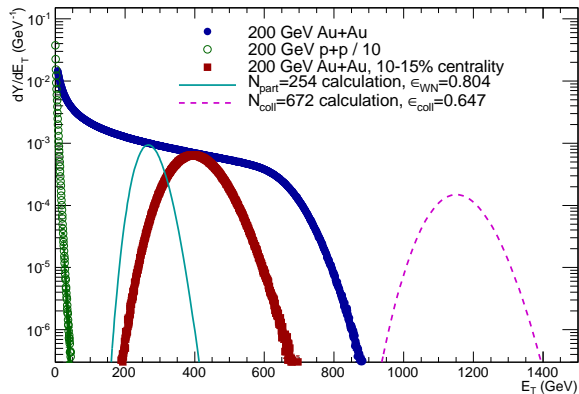


FIG. 18: (Color online) Au+Au measurement of $dE_T/d\eta$, with 10%–15% centrality region indicated, compared to the calculation of the distribution given by Eq. 21 for $N_{\text{part}}=254$ and $N_{\text{coll}}=672$ corresponding to 10%–15% centrality.

computing Eq. 6 on an event-by-event basis as a nuclear geometry distribution in a standard Glauber calculation, agrees very well with their measured E_T distribution in the pseudorapidity range $3.2 < |\eta| < 4.9$ at $\sqrt{s_{NN}}=2.76$ TeV Pb+Pb collisions. Similar results were obtained by ALICE [81]. This confirms the observation noted previously (Sec. VI) that the success of the two component model is not because there are some contributions proportional to N_{part} and some proportional to N_{coll} , but rather because a particular linear combination of N_{part} and N_{coll} turns out to be an empirical proxy for the nuclear geometry of the number of constituent-quark participants, N_{qp} in A+A collisions.

X. SUMMARY

To summarize, the midrapidity transverse energy distributions, $dE_T/d\eta$, have been measured for $\sqrt{s_{NN}}=200$ GeV $p+p$ and $d+Au$ collisions, and for Au+Au collisions at $\sqrt{s_{NN}}=200, 130,$ and 62.4 GeV. As a function of centrality, the $\langle dE_T/d\eta \rangle$ measured in Au+Au collisions at all three collision energies exhibit a nonlinear increase with increasing centrality when expressed as the number of nucleon participants, N_{part} . When expressed in terms of the number of constituent-quark participants, N_{qp} , the $\langle dE_T/d\eta \rangle$ increases linearly with N_{qp} . Several Extreme Independent models of particle production have been compared to the data, including calculations based upon color-strings (the Additive Quark Model, AQM) and the constituent-Quark Participant model (NQP). When compared to data from symmetric systems (Au+Au and $p+p$), these two models cannot generally be distinguished from each other. In the present measurement, the different detection efficiency for a quark-participant and color string in the two cases allows a separation, with the NQP model favored. However, when compared to data from the asymmetric $d+Au$ system, the $d+Au$ measurement clearly rejects the AQM model and agrees very well with the NQP model. This implies that transverse energy production at midrapidity in relativistic heavy ion collisions is well described by particle production based upon the number of constituent-quark participants. Additional support for this conclusion is that the ansatz, $[(1-x)\langle N_{\text{part}} \rangle/2 + x\langle N_{\text{coll}} \rangle]$, which has been used successfully to represent the nonlinearity of $\langle dE_T/d\eta \rangle$ as a function of N_{part} , turns out to be simply a proxy for $\langle N_{qp} \rangle$ in A+A collisions and does not represent a hard-scattering component in E_T distributions.

ACKNOWLEDGMENTS

We thank the staff of the Collider-Accelerator and Physics Departments at Brookhaven National Laboratory and the staff of the other PHENIX participating institutions for their vital contributions. We acknowledge support from the Office of Nuclear Physics in the Office of Science of the Department of Energy, the National Science Foundation, Abilene Christian University Research Council, Research Foundation of SUNY, and Dean of the College of Arts and Sciences, Vanderbilt University (U.S.A), Ministry of Education, Culture, Sports, Science, and Technology and the Japan Society for the Promotion of Science (Japan), Conselho Nacional de Desenvolvimento Científico e Tecnológico and Fundação de Amparo à Pesquisa do Estado de São Paulo (Brazil), Natural Science Foundation of China (P. R. China), Centre National de la Recherche Scientifique, Commissariat à l'Énergie

Atomique, and Institut National de Physique Nucléaire et de Physique des Particules (France), Bundesministerium für Bildung und Forschung, Deutscher Akademischer Austausch Dienst, and Alexander von Humboldt Stiftung (Germany), Hungarian National Science Fund, OTKA (Hungary), Department of Atomic Energy (India), Israel Science Foundation (Israel), National Research Foundation and WCU program of the Ministry Education Science and Technology (Korea), Physics Department, Lahore University of Management Sciences (Pakistan), Ministry of Education and Science, Russian Academy of Sciences, Federal Agency of Atomic Energy (Russia), VR and Wallenberg Foundation (Sweden), the U.S. Civilian Research and Development Foundation for the Independent States of the Former Soviet Union, the US-Hungarian NSF-OTKA-MTA, and the US-Israel Binational Science Foundation.

-
- [1] K. Adcox et al. (PHENIX Collaboration), *Phys. Rev. Lett.* **87**, 052301 (2001).
- [2] S. S. Adler et al. (PHENIX Collaboration), *Phys. Rev. C* **71**, 034908 (2005).
- [3] X.-N. Wang and M. Gyulassy, *Phys. Rev. Lett.* **86**, 3496 (2001).
- [4] D. Kharzeev and M. Nardi, *Phys. Lett. B* **507**, 121 (2001).
- [5] S. Eremín and S. Voloshin, *Phys. Rev. C* **67**, 064905 (2003).
- [6] A. Bialas, W. Czyz, and L. Lesniak, *Phys. Rev. D* **25**, 2328 (1982).
- [7] T. Ochiai, *Z. Phys. C* **35**, 209 (1987).
- [8] U. Camerini, W. O. Lock, and D. Perkins, in *Progress in Cosmic Ray Physics*, edited by J. G. Wilson (North Holland, Amsterdam, 1952), vol. I, pp. 1–34.
- [9] G. Cocconi, L. J. Koester, and D. H. Perkins, *Tech. Rep. UCRL-10022* (1961), Lawrence Radiation Laboratory (1961), p. 167, as cited by Ref. [10].
- [10] J. Orear, *Phys. Rev. Lett.* **12**, 112 (1964).
- [11] A. H. Mueller, *Phys. Rev. D* **4**, 150 (1971).
- [12] Z. Koba, H. B. Nielsen, and P. Olesen, *Nucl. Phys. B* **40**, 317 (1972).
- [13] G. Arnison et al., *Phys. Lett. B* **107**, 320 (1981).
- [14] G. J. Alner et al., *Phys. Rpts.* **154**, 247 (1987).
- [15] For instance, see Maurice Jacob's Eulogy for the ISR in CERN report 84-13, (CERN, SIS, Geneva 1984).
- [16] W. Thomé et al., *Nucl. Phys.* **B129**, 365 (1977).
- [17] G. N. Fowler and R. M. Weiner, *Phys. Lett. B* **70**, 201 (1977).
- [18] W. J. Willis, in *ISABELLE Physics Prospects (BNL-17522)*, edited by R. B. Palmer (Brookhaven National Laboratory, Upton, NY, 1972), pp. 207–234, (n.b. same report appears as CRISP-72-15, BNL-16841).
- [19] J. D. Bjorken, *Phys. Rev. D* **8**, 4098 (1973).
- [20] W. Ochs and L. Stodolsky, *Phys. Lett. B* **69**, 225 (1977).
- [21] P. V. Landshoff and J. C. Polkinghorne, *Phys. Rev. D* **18**, 3344 (1978).
- [22] C. De Marzo et al. (Bari-Cracow-Liverpool-Munich-Nijmegen), *Phys. Lett. B* **112**, 173 (1982).
- [23] G. Arnison et al. (UA1), *Transverse energy distributions in the central calorimeters*, presented to 21st Int. Conf. High Energy Physics, Paris, France, Jul 26-31, 1982, CERN-EP-82-122. (Unpublished). Also see reference [13].
- [24] J.-P. Repellin et al., in *Proc. 21st Int. Conf. High Energy Physics (Paris)*, edited by P. Petiau and M. Porneuf (*Journal de Physique Colloques*, Paris, 1982), vol. 43, pp. C3-571 – C3-578.
- [25] J. A. Appel et al., *Phys. Lett. B* **165**, 441 (1985).
- [26] J. D. Bjorken, *Phys. Rev. D* **27**, 140 (1983).
- [27] W. Busza et al., *Phys. Rev. Lett.* **34**, 836 (1975).
- [28] C. Halliwell et al., *Phys. Rev. Lett.* **39**, 1499 (1977).
- [29] P. M. Fishbane and J. S. Trefil, *Phys. Rev. D* **9**, 168 (1974).
- [30] P. M. Fishbane and J. S. Trefil, *Phys. Lett. B* **51**, 139 (1974).
- [31] K. Gottfried, *Phys. Rev. Lett.* **32**, 957 (1974).
- [32] A. S. Goldhaber, *Phys. Rev. D* **7**, 765 (1973).
- [33] A. Białas and W. Czyż, *Phys. Lett. B* **51**, 179 (1974).
- [34] B. Andersson and I. Otterlund, *Nucl. Phys. B* **88**, 349 (1975).
- [35] S. Frankel, *Phys. Rev. C* **48**, R2170 (1993).
- [36] A. Białas, M. Bleszyński, and W. Czyż, *Nucl. Phys. B* **111**, 461 (1976).
- [37] L. Ahle et al., *Phys. Rev. C* **57**, R466 (1998).
- [38] J. Ftacnik, K. Kajantie, N. Pisutova, and J. Pisut, *Phys. Lett. B* **188**, 279 (1987).
- [39] T. Abbott et al., *Phys. Lett. B* **197**, 285 (1987).
- [40] T. Abbott et al., *Phys. Rev. C* **63**, 064602 (2001).
- [41] A. L. S. Angelis et al., *Phys. Lett. B* **141**, 140 (1984).
- [42] T. Åkesson et al., *Phys. Lett. B* **231**, 359 (1989).
- [43] A. Bamberger et al., *Phys. Lett. B* **184**, 271 (1987).
- [44] L. P. Remsberg et al., *Z. Phys. C* **38**, 35 (1988).
- [45] B. Alver et al., *Phys. Rev. C* **83**, 024913 (2011).
- [46] K. Adcox et al. (PHENIX Collaboration), *Phys. Rev. Lett.* **86**, 3500 (2001).
- [47] R. Nouicer, *Eur. Phys. J. C* **49**, 281 (2007).
- [48] B. De and S. Bhattacharyya, *Phys. Rev. C* **71**, 024903

- (2005).
- [49] A. Bialas, J. Phys. **G 35**, 044053 (2008).
- [50] M. Gell-Mann, Phys. Lett. **8**, 214 (1964).
- [51] R. P. Feynman, M. Gell-Mann, and G. Zweig, Phys. Rev. Lett. **13**, 678 (1964).
- [52] G. Morpurgo, Annu. Rev. Nucl. Part. Sci. **20**, 105 (1970).
- [53] J. J. J. Kokkedee, *THE QUARK MODEL* (W. A. Benjamin, Inc., New York, 1969).
- [54] E. V. Shuryak, Nucl. Phys. B **203**, 116 (1982).
- [55] D. Diakonov, Prog. Part. Nucl. Phys. **36**, 1 (1996).
- [56] S. Weinberg, Eur. Phys. J. C **34**, 5 (2004).
- [57] V. V. Anisovich, Y. M. Shabelsky, and V. M. Shekhter, Nucl. Phys. B **133**, 477 (1978).
- [58] R. C. Hwa, Phys. Rev. D **22**, 759 (1980).
- [59] T. Akiba, Phys. Lett. B **109**, 477 (1982).
- [60] E. M. Levin and L. L. Frankfurt, JETP Lett. **2**, 66 (1965).
- [61] H. J. Lipkin, Phys. Rev. Lett. **16**, 1015 (1966).
- [62] K. Adcox et al. (PHENIX Collaboration), Nucl. Instrum. Methods A **499**, 469 (2003).
- [63] M. Allen et al. (PHENIX Collaboration), Nucl. Instrum. Methods A **499**, 549 (2003).
- [64] A. Adare et al. (PHENIX Collaboration), Phys. Rev. **C86**, 064901 (2012).
- [65] X.-N. Wang and M. Gyulassy, Phys. Rev. D **44**, 3501 (1991).
- [66] S. S. Adler et al. (PHENIX Collaboration), Phys. Rev. Lett. **98**, 172302 (2007).
- [67] L. Aphecetche et al. (PHENIX Collaboration), Nucl. Instrum. Methods A **499**, 521 (2003).
- [68] M. L. Miller, K. Reygers, S. J. Sanders, and P. Steinberg, Ann. Rev. Nucl. Part. Sci. **57**, 205 (2007).
- [69] R. Hofstadter, F. Bumiller, and M. R. Yerian, Rev. Mod. Phys. **30**, 482 (1958).
- [70] K. Aamodt et al., Phys. Rev. Lett. **106**, 032301 (2011).
- [71] K. Adcox et al. (PHENIX Collaboration), Phys. Rev. Lett. **88**, 022301 (2002).
- [72] B. Back et al., Phys. Rev. C **70**, 021902(R) (2004).
- [73] M. J. Tannenbaum, Phys. Rev. C **69**, 064902 (2004).
- [74] A. L. S. Angelis et al., Phys. Lett. B **126**, 132 (1983).
- [75] L. Aphecetche et al., Nucl. Inst. Methods A **499**, 521 (2003).
- [76] For example see Fig. 6 in reference [77].
- [77] M. J. Tannenbaum, Rep. Prog. Phys. **69**, 2005 (2006).
- [78] S. S. Adler et al. (PHENIX Collaboration), Phys. Rev. Lett. **91**, 241803 (2003).
- [79] S. S. Adler et al. (PHENIX Collaboration), Phys. Rev. Lett. **98**, 012002 (2007).
- [80] G. Aad et al., Phys. Lett. B **707**, 330 (2012).
- [81] B. Abelev et al., Phys. Rev. C **88**, 044909 (2013).